J. Fluid Mech. (2019), *vol.* 862, *pp.* 1105–1134. © Cambridge University Press 2019
doi:10.1017/jfm.2018.968

Bubble cloud dynamics in an ultrasound field

Kazuki Maeda[1,†] **and Tim Colonius**[1]

[1]Division of Engineering and Applied Science, California Institute of Technology, Pasadena, CA 91125, USA

(Received 1 May 2018; revised 15 September 2018; accepted 16 November 2018; first published online 16 January 2019)

The dynamics of bubble clouds induced by high-intensity focused ultrasound is investigated in a regime where the cloud size is similar to the ultrasound wavelength. High-speed images show that the cloud is asymmetric; the bubbles nearest the source grow to a larger radius than the distal ones. Similar structures of bubble clouds are observed in numerical simulations that mimic the laboratory experiment. To elucidate the structure, a parametric study is conducted for plane ultrasound waves with various amplitudes and diffuse clouds with different initial void fractions. Based on an analysis of the kinetic energy of liquid induced by bubble oscillations, a new scaling parameter is introduced to characterize the dynamics. The new parameter generalizes the cloud interaction parameter originally introduced by d'Agostino & Brennen (*J. Fluid Mech.*, vol. 199, 1989, pp. 155–176). The dynamic interaction parameter controls the energy localization and consequent anisotropy of the cloud. Moreover, the amplitude of the far-field, bubble-scattered acoustics is likewise correlated with the proposed parameter. Findings of the present study not only shed light on the physics of cloud cavitation, but may also be of use for the quantification of the effects of cavitation on outcomes of ultrasound therapies including high-intensity focused ultrasound-based lithotripsy.

Key words: bubble dynamics, cavitation

1. Introduction

The dynamics of cavitation bubble clouds excited in an intense ultrasound field is of critical importance for the safety and efficacy of lithotripsy and high-intensity focused ultrasound (HIFU). In such therapy, cavitation bubbles can be formed in the human body during the passage of the tensile part of ultrasound pulses. Bubbles can scatter and absorb subsequent pulses, and the violent collapse of bubbles can cause cavitation damage (Coleman *et al.* 1987; Pishchalnikov *et al.* 2003; Matsumoto *et al.* 2005; McAteer *et al.* 2005; Ikeda *et al.* 2006; Bailey *et al.* 2006; Stride & Coussios 2010; Miller *et al.* 2012). Due to the short time scale and three-dimensional nature of cloud cavitation, precise measurement of individual bubbles has been challenging. Numerical simulations using mixture-averaging approaches (vanWijngaarden 1968; Biesheuvel & vanWijngaarden 1984) have remained central tools for quantification of the dynamics of bubble clouds.

† Present address: Department of Mechanical Engineering, University of Washington, Seattle, WA 98195, USA. Email address for correspondence: kazuki.e.maeda@gmail.com

https://doi.org/10.1017/jfm.2018.968 Published online by Cambridge University Press

Early studies of bubble cloud dynamics focused on assessment of cavitation noise and erosion of materials. Mørch (1980, 1982) theoretically modelled the inward-propagating collapse of spherical bubble clusters and quantified the resulting collapse pressure. Omta (1987) studied acoustic emission from a spherical bubble cloud excited by step change of pressure in the surrounding liquid. d'Agostino & Brennen (1989) formulated the linearized dynamics of monodisperse, spherical bubble clouds under weak, long-wavelength pressure excitation and identified that the cloud interaction parameter, $B = \beta R_c^2/R_{b0}^2$, dictates the linear dynamics of the cloud, where β is the void fraction and R_c and R_{b0} are the initial radius of the cloud and the bubbles, respectively. Wang & Brennen (1994, 1999) extended the study to the nonlinear regime, further characterizing the strong collapse of bubble clouds accompanied by a shock wave. Shimada, Matsumoto & Kobayashi (2000) used a similar approach to assess the effect of the polydispersity of nuclei on the nonlinear dynamics of spherical bubble clouds.

Later, numerical studies of cavitation attracted interest for medical applications. Tanguay (2003) extended the mixture-averaging approach to simulate and characterize the dynamics of cavitation bubble clouds induced in extra-corporeal shock wave lithotripsy (ESWL). Matsumoto & Yoshizawa (2005) extended the method of Shimada *et al.* (2000) to quantify amplifications in the pressure due to bubble cloud collapse under excitation by resonant HIFU waves and discussed applications of the collapse energy to kidney stone comminution as an alternative method of ESWL.

In experiments, Reisman, Wang & Brennen (1998) used high-speed imaging to observe cloud cavitation collapse on a finite-span hydrofoil, and analysed acoustic signals from the cloud collapse, and associated the results with the inward-propagating shock wave predicted in the aforementioned studies. Arora, Ohl & Lohse (2007) observed collapse in bubble clouds of controlled nuclei concentration, and observed an inward-propagating collapse with high nuclei concentrations. Lu, Katz & Prosperetti (2013) studied the spatial distribution and the translational motions of bubble clouds in standing acoustic waves on a time scale longer than that of the collapse.

The aforementioned theoretical studies focus on bubble clouds in an otherwise incompressible liquid so that the wavelength of the pressure excitation is much larger than the size of the cloud. In practical conditions of ultrasound therapies, however, the scale separation invoked above does not hold. In fact, Maeda *et al.* (2015) observed bubble clouds with a size of the order of a millimetre *in vitro* during the passage of a strong ultrasound wave with a wavelength as short as the cloud size.

As a representative example of such bubble clouds, in figure 1 we show the evolution of an isolated bubble cloud nucleated in a pulse of focused ultrasound consisting of 10 wavelengths with a carrier frequency of $f = 335$ kHz, thus a wavelength of $\lambda = 4.4$ mm, generated by a medical transducer in water. The experiment, extended from a set-up documented in Maeda *et al.* (2015), is designed to characterize the dynamics of bubble clouds in a recently proposed HIFU-based lithotripsy, burst wave lithotripsy (Maxwell *et al.* 2015). Details of the experimental set-up are described in appendix A. The cloud is growing up through the 10th frame, as the ultrasound wave is propagating through the focal region, and then decays in the subsequent frames. The bubble cloud occupies an approximately spherical volume with $R_c \approx 2.5$ mm. The size of the bubble cloud is thus at the same scale as the wavelength of the incident wave. Notably, the cloud possesses an anisotropic structure in that the proximal bubbles grow to a larger radius than the distal bubbles. This dynamics is significantly different from that of bubble clouds in the long-wavelength regime.

https://doi.org/10.1017/jfm.2018.968 Published online by Cambridge University Press

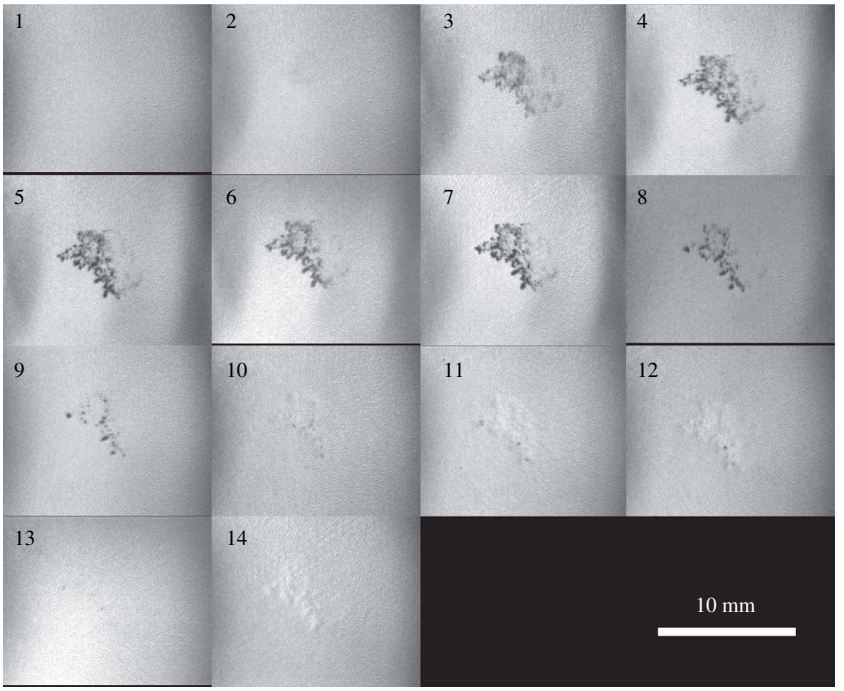


FIGURE 1. High-speed images showing evolution of a representative bubble cloud excited by a focused ultrasound wave in the short-wavelength regime. The wave propagates from the left to the right. The grey shadows with a shape of the bubble cloud present in the 11th to the 14th frames are an artifact of the imaging system.

Advanced interface capturing methods are capable of simulating detailed dynamics of each bubble in a cloud in a compressible liquid at fine spatial scales, and have been applied to bubble cloud collapse in a free field by Rossinelli *et al.* (2013) and Rasthofer *et al.* (2017) and near a wall by Tiwari, Pantano & Freund (2015). Yet, such methods are still computationally intensive and applications are limited to the dynamics within a short time scale, typically that of a single cycle of bubble collapse. For more complex problems, modelling assumptions have to be made to reduce the computational cost. In this spirit, we have recently developed a method that enables simulation of cloud cavitation in an intense ultrasound field with a fine spatial resolution without a constraint of scale separation (Maeda & Colonius 2018). The method solves mixture-averaged equations using an Eulerian–Lagrangian approach (Kameda & Matsumoto 1996; Fuster & Colonius 2011; Ma, Chahine & Hsiao 2015; Ma, Hsiao & Chahine 2018). The bubble mixture is discretized on an Eulerian grid, while the individual bubbles are tracked on Lagrangian points and their radial dynamics are solved using the Keller–Miksis equation. By doing so, the dynamics of each bubble and that of the bubble-scattered pressure wave are accurately captured with a reasonable computational expense.

Our simulation successfully reproduces the aforementioned inward-propagating spherical cloud collapse in the long-wavelength regime. Figure 2 shows the evolution of bubbles with an initial radius of 10 μm that are randomly distributed within a sphere of radius 2.5 mm and excited by a single cycle of a planer sinusoidal wave with a frequency of 50 kHz, thus a wavelength of 30 mm, and an amplitude of 1 MPa.

https://doi.org/10.1017/jfm.2018.968 Published online by Cambridge University Press

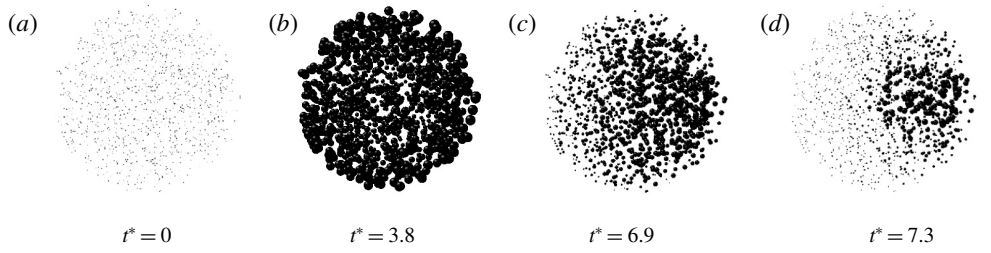


FIGURE 2. Evolution of a bubble cloud excited by a single cycle of sinusoidal wave in the long-wavelength regime. The wave propagates from the left to the right, with a frequency of $f = 50$ kHz, thus a wavelength of 30 mm, and an amplitude of 1 MPa. Parameter t^* denotes non-dimensional time, where $t^* = tf$.

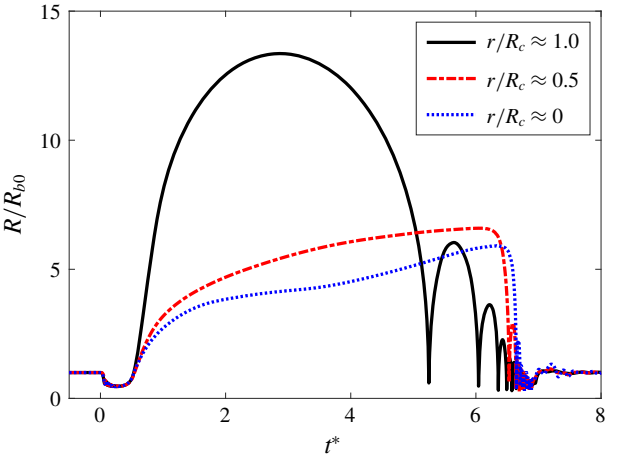


FIGURE 3. (Colour online) Evolution of the normalized radii of three bubbles at distinct locations in the cloud shown in figure 2. Parameter r denotes the distance from the cloud centre.

The wavelength is much longer than the cloud size and this effectively models the scale separation. Figure 3 shows the evolution of the radii of representative bubbles that are initially located at three distinct radial coordinates of the cloud: cloud centre; mid-point between the centre and the cloud periphery; and periphery. The peripheral bubble grows to a larger maximum radius and collapses faster than the other bubbles, while the inner bubbles are subsequently collapsed during the arrival of the inward-propagating bubbly shock wave. The result qualitatively reproduces the numerical simulation of Wang & Brennen (1994, 1999) as well as the experimental observation of Arora *et al.* (2007).

Motivated by high-speed imaging and preliminary simulation, in this paper we aim to use numerical simulations to provide a first insight into the bubble clouds excited by HIFU where the cloud radius is commensurate with the wavelength.

The paper is organized as follows. In § 2 we provide a summary of the modelling and numerical methods. In § 3 we introduce metrics to quantify the dynamics of bubble clouds, including the cloud interaction parameter introduced by d'Agostino & Brennen (1989), and moments of the volume and the kinetic energy. In § 4 we simulate the dynamics of bubble clouds excited by a focused ultrasound wave with various polydispersities and populations of nuclei in a set-up that mimics the

https://doi.org/10.1017/jfm.2018.968 Published online by Cambridge University Press

experimental conditions. We quantitatively compare results with the experimental high-speed images shown in figure 1 and evaluate the anisotropic structure. To further elucidate the dynamics in more generalized conditions, in § 5 we conduct a parametric study of bubble clouds excited by a plane ultrasound wave, varying the nuclei populations and the amplitudes of the wave. In § 5.2 we quantitatively analyse the anisotropic structure, and in § 5.3 we propose a new scaling parameter to characterize the dynamics of the clouds by generalizing the cloud interaction parameter of d'Agostino & Brennen (1989). In § 5.4 we collapse the moments of bubble-induced kinetic energy in terms of the proposed parameter and identify the mechanisms by which energy is localized in the proximal side of the cloud. In § 5.5 the amplitude and directionality of the scattered acoustic field are evaluated and collapsed by the proposed parameter. The energy localization and the scattered acoustics are directly correlated. In § 6 we discuss implications of the numerical results for the effects of cloud cavitation on outcomes of HIFU-based lithotripsy. In § 7 we state conclusions.

2. Model formulation

2.1. *Bubble cloud dynamics*

Here we briefly summarize the physical model and numerical method for simulation of cloud cavitation utilized in the present study. Further details are available in Maeda & Colonius (2017). The method employs a two-way coupled Eulerian–Lagrangian approach. We describe the dynamics of bubbly mixture using volume-averaged equations of motion (Caflisch *et al.* 1985; Commander & Prosperetti 1989):

$$\frac{\partial \overline{\rho}}{\partial t} + \boldsymbol{\nabla} \cdot (\overline{\rho \boldsymbol{u}}) = 0, \tag{2.1}$$

$$\frac{\partial (\overline{\rho \boldsymbol{u}})}{\partial t} + \boldsymbol{\nabla} \cdot (\overline{\rho \boldsymbol{u}} \otimes \overline{\boldsymbol{u}} + p\mathcal{I} - \mathcal{T}) = 0, \tag{2.2}$$

$$\frac{\partial \overline{E}}{\partial t} + \boldsymbol{\nabla} \cdot ((\overline{E} + p)\overline{\boldsymbol{u}} - \mathcal{T} \cdot \overline{\boldsymbol{u}}) = 0, \tag{2.3}$$

where ρ is the density, $\boldsymbol{u} = (u, v, w)^{\mathrm{T}}$ is the velocity, p is the pressure and E is the total energy. Here, $\overline{(\cdot)}$ denotes the volume-averaging operator: $\overline{(\cdot)} = (1-\beta)(\cdot)_l + \beta(\cdot)_g$, where $\beta \in [0, 1)$ is the volume fraction of gas (void fraction), and subscripts l and g denote the liquid and gas phase, respectively. Here, $\mathcal{T}$ is the effective viscous stress tensor of the mixture, which we approximate as that of the liquid phase: $\mathcal{T} \approx \mathcal{T}_l$. We invoke two approximations valid at the limit of low void fraction: the density of the mixture is approximated by that of the liquid: $\overline{\rho} \approx (1-\beta)\rho_l$; and the slip velocity between the two phases is zero: $\overline{\boldsymbol{u}} \approx \boldsymbol{u}_l = \boldsymbol{u}_g$.

Equations (2.1)–(2.3) can be rewritten as conservation equations in terms of the mass, momentum and energy of the liquid with source terms, as an inhomogeneous hyperbolic system:

$$\frac{\partial \rho_l}{\partial t} + \boldsymbol{\nabla} \cdot (\rho_l \boldsymbol{u}_l) = \frac{\rho_l}{1-\beta}\left[\frac{\partial \beta}{\partial t} + \boldsymbol{u}_l \cdot \boldsymbol{\nabla}\beta\right], \tag{2.4}$$

$$\frac{\partial (\rho_l \boldsymbol{u}_l)}{\partial t} + \boldsymbol{\nabla} \cdot (\rho_l \boldsymbol{u}_l \otimes \boldsymbol{u}_l + p\mathcal{I} - \mathcal{T}_l) = \frac{\rho_l \boldsymbol{u}}{1-\beta}\left[\frac{\partial \beta}{\partial t} + \boldsymbol{u}_l \cdot \boldsymbol{\nabla}\beta\right] - \frac{\beta \boldsymbol{\nabla} \cdot (p\mathcal{I} - \mathcal{T}_l)}{1-\beta}, \tag{2.5}$$

https://doi.org/10.1017/jfm.2018.968 Published online by Cambridge University Press

$$\frac{\partial E_l}{\partial t} + \boldsymbol{\nabla} \cdot ((E_l + p)\boldsymbol{u}_l - \mathcal{T}_l \cdot \boldsymbol{u}_l) = \frac{E_l}{1-\beta}\left[\frac{\partial \beta}{\partial t} + \boldsymbol{u}_l \cdot \boldsymbol{\nabla}\beta\right] - \frac{\beta \boldsymbol{\nabla} \cdot (p\boldsymbol{u}_l - \mathcal{T}_l \cdot \boldsymbol{u}_l)}{1-\beta}. \tag{2.6}$$

For a thermodynamic closure for the liquid, we employ stiffened gas equation of state:

$$p = (\gamma - 1)\rho\varepsilon - \gamma\pi_\infty, \tag{2.7}$$

where $\varepsilon = E_l - \rho_l \boldsymbol{u}_l^2/2$ and is the internal energy of liquid, γ is the specific heat ratio and π_∞ is the stiffness. In the present study we use $\gamma = 7.1$ and $\pi_\infty = 3.06 \times 10^8$ Pa for water. Stiffened gas equation of state well models the thermodynamics of liquid under high pressure and has been widely used in simulation of fully compressible gas–liquid flows that involve shock and strong pressure waves (Menikoff & Plohr 1989; Shyue 1998; Coralic & Colonius 2014; Tiwari *et al.* 2015; Rasthofer *et al.* 2017).

At the limit of small change in the density of liquid, the equation of state can be linearized as

$$p = p_0 + c_0^2(\rho - \rho_0), \tag{2.8}$$

where

$$c = \sqrt{\gamma(p + \pi_\infty)/\rho} \tag{2.9}$$

is the speed of sound in liquid and the subscript 0 denotes reference states. With $\rho_0 = 1000\ \mathrm{m^3\ kg^{-1}}$, we recover an ambient speed of sound in water, $c_0 = 1475\ \mathrm{m\ s^{-1}}$.

To model the gas phase, we employ a Lagrangian point-bubble approach, in that the gas phase is treated as spherical, radially oscillating cavities consisting of a non-condensible gas and liquid vapour. The centre of the nth bubble ($n \in \mathbb{Z} : n \in [1, N]$), with a radius of R_n and a radial velocity of $\dot{R}_n$, is initially defined at the coordinate $\boldsymbol{x}_n$ and tracked as Lagrangian points during simulations. To define the continuous field of the void fraction in the mixture at coordinate $\boldsymbol{x}$, we smear the volume of bubble using a regularization kernel δ:

$$\beta(\boldsymbol{x}) = \sum_{n=1}^{N} V_n(R_n)\delta(d_n, h), \tag{2.10}$$

where V_n is the volume of bubble n, $V_n = 4\pi/3R_n^3$, and d_n is the distance of the coordinate $\boldsymbol{x}$ from the centre of the bubble, $d_n = |\boldsymbol{x} - \boldsymbol{x}_n|$. We discretize equations (2.4)–(2.6) on an axisymmetric grid. The Lagrangian bubbles are distributed in three-dimensional space. The kernel δ maps the volume of bubbles onto the void fraction field defined on axisymmetric coordinates with a kernel width of h. In the present study, we use $h = 1.1\Delta x$, where Δx is the characteristic width of the computational cell that encloses the bubble. The averaged inter-bubble distance is larger than the size of bubbles as well as h. The bubbles, while three-dimensional, are forced by the axisymmetric pressure field, which is appropriate to obtain spatially averaged quantities of the bubbles addressed in the present study (Maeda & Colonius 2017). Spatial integration is realized using a fifth-order finite-volume weighted essentially non-oscillatory scheme (Coralic & Colonius 2014). A fourth-/fifth-order Runge–Kutta–Cash–Karp algorithm (Cash & Karp 1990) is employed for time integration of solutions.

To model the dynamics of volumetric oscillations of bubbles, we employ the Keller–Miksis equation (Keller & Miksis 1980):

$$\left(R_n\left(1 - \frac{\dot{R}_n}{c}\right)\right)\ddot{R}_n + \frac{3}{2}\dot{R}^2\left(1 - \frac{\dot{R}_n}{3c}\right) = \frac{p_n - p_\infty}{\rho}\left(1 + \frac{\dot{R}_n}{c}\right) + \frac{R_n\dot{p}_n}{\rho c}, \tag{2.11}$$

https://doi.org/10.1017/jfm.2018.968 Published online by Cambridge University Press

$$p_n = p_{Bn} - \frac{4\mu_l \dot{R}_n}{R_n} - \frac{2\sigma_s}{R_n}, \tag{2.12}$$

where p_n is the pressure at the bubble wall, p_{Bn} is the pressure inside the bubble, σ_s is the surface tension and p_∞ is the component of the pressure that forces the radial oscillations of the bubble. Pressure p_∞ is obtained by a sub-grid-scale model as a function of p_n and the pressure of the grid cells surrounding bubble n. To close the equation, we consider conservation equations inside the bubble. To do so, we utilize a reduced-order model introduced by Preston, Colonius & Brennen (2007) to account for the effect of heat transfer, and mass transfer due to evaporation and condensation of vapour across the bubble–liquid interface. A brief remark on the closure is given in appendix B. The model does not account for fusion, fission or non-spherical deformation of bubbles. In diffuse bubble clouds considered in the present study, the averaged inter-bubble distance is so long that fusion of bubbles may be a rare event, while fission and non-spherical deformation may occur at the moment of violent collapse of bubbles (Brennen 2002). We know of no way to account for such effects save directly simulating all the bubbles, which would be prohibitively expensive for the present cloud.

2.2. *Acoustic source*

In simulations we excite volumetric oscillations of bubbles using plane and focused pressure waves. In order to generate the waves in the computational domain, we utilize a source-term approach introduced by Maeda & Colonius (2017). The method can generate uni-directional acoustic waves from an arbitrarily chosen source surface, by forcing the mass, momentum and energy equations (2.4)–(2.6) in a thin volume enclosing the surface.

3. Theory and scaling for the dynamics of bubble clouds

3.1. *Cloud interaction parameter*

d'Agostino & Brennen (1989) (hereafter DB) studied the linear response of monodisperse, spherical bubble clouds subjected to harmonic, long-wavelength pressure excitation. DB deduced that the response of the bubble cloud with a low void fraction is characterized by a non-dimensional parameter,

$$B_0 = \frac{\beta_0 R_c^2}{R_{b0}^2}, \tag{3.1}$$

termed as the cloud interaction parameter. DB found that, when $B_0 \ll 1$, the effect of inter-bubble interaction is weak and each bubble in the cloud behaves like a single, isolated bubble. When $B_0 \gg 1$, inter-bubble interactions cause bubbles to oscillate coherently at a lower frequency than an isolated single bubble. Wang & Brennen (1999) simulated the dynamics of a spherical bubble cloud with various values of B_0 in the nonlinear regime.

The cloud interaction parameter can be interpreted in different ways. Substituting $\beta = N_b R_{b0}^3 / R_c^3$ into (3.1), B_0 can be rewritten as

$$B_0 = \frac{N_b R_{b0}^3}{R_c^3} \frac{R_c^2}{R_{b0}^2} = \frac{N_b R_{b0}}{R_c}, \tag{3.2}$$

https://doi.org/10.1017/jfm.2018.968 Published online by Cambridge University Press

where N_b is the number of bubbles in the cloud. We notice that this scaling parameter can be independently derived from the Lagrangian mechanics of spherical bubbles under mutual interactions. The global kinetic energy of potential flow of an incompressible liquid induced by volumetric oscillations of N_b spherical bubbles can be expressed using a multipole expansion (Takahira, Akamatsu & Fujikawa 1994; Ilinskii, Hamilton & Zabolotskaya 2007) as

$$K = 2\pi\rho_l \left[\sum_{i}^{N_b} R_i^3 \dot{R}_i^2 + \sum_{i}^{N_b} \sum_{j}^{N_b} \frac{R_i^2 R_j^2 \dot{R}_i \dot{R}_j}{r_{i,j}} + O\left(\frac{R^7 \dot{R}^2}{r^4} \right) \right], \tag{3.3}$$

where $r_{i,j}$ is the distance between the centres of bubble i and bubble j. The first term in the brackets represents the kinetic energy induced by direct contributions from each bubble and the second term represents the energy induced by the inter-bubble interactions. When bubbles have an approximately uniform size distribution and experience simultaneous change in pressure, we can assume that each bubble takes the same characteristic radius and velocity, R and $\dot{R}$. The characteristic inter-bubble distance can be scaled as $r \sim R_c$. Then K can be scaled as

$$K \sim \rho_l N_b R^3 \dot{R}^2 \left(1 + \frac{N_b R}{R_c} \right). \tag{3.4}$$

In the limit of small-amplitude oscillations we have $R \approx R_{b0}$, and therefore we obtain

$$K \sim \rho_l N_b R_{b0}^3 \dot{R}^2 \, (1 + B_0) \, . \tag{3.5}$$

We see that the interaction parameter dictates the kinetic energy induced by bubbles. With $B_0 = 0$ the kinetic energy is that of N_b isolated bubbles, while with $B_0 > 1$ there is an additional contribution from the inter-bubble interactions. Based on equation (3.3), an extended Rayleigh–Plesset equation for the dynamics of the bubbles can be derived (Chahine 1983; Takahira *et al.* 1994; Doinikov 2004; Bremond *et al.* 2006; Ilinskii *et al.* 2007; Zeravcic, Lohse & Van Saarloos 2011). In fact, the scaling of kinetic energy in terms of $N_b R_b / R_c$ was mentioned by Ilinskii *et al.* (2007), but was not associated with the parameter derived by DB.

In what follows we specify the size distribution of nuclei to be a log-normal distribution given by $\ln(R_b/R_{b,ref}) \sim N(0, \sigma^2)$. Therefore we employ the following expression for B_0:

$$B_0 \approx \frac{N_b R_{b0,ref}}{R_c}. \tag{3.6}$$

3.2. *Moments*

In order to quantify the anisotropic structure and associated bubble dynamics, we use the moments of either bubble volume or kinetic energy of the liquid, both measured with respect to the initial centre of the cloud (hereafter denoted as the moment of volume and moment of kinetic energy, respectively). The nth moments of the bubble volume and the bubble-induced kinetic energy of liquid are thus respectively defined as

$$\mu_{Vcn} = \frac{\displaystyle\sum_{bubble} \frac{4\pi}{3} R_b^3 \left(\frac{x_b}{R_c} \right)^n}{\displaystyle\sum_{bubble} \frac{4\pi}{3} R_b^3} \quad \text{and} \quad \mu_{Kcn} = \frac{\displaystyle\sum_{bubble} 2\pi\rho R_b^3 \dot{R}_b^2 \left(\frac{x_b}{R_c} \right)^n}{\displaystyle\sum_{bubble} 2\pi\rho R_b^3 \dot{R}_b^2}. \tag{3.7a,b}$$

https://doi.org/10.1017/jfm.2018.968 Published online by Cambridge University Press

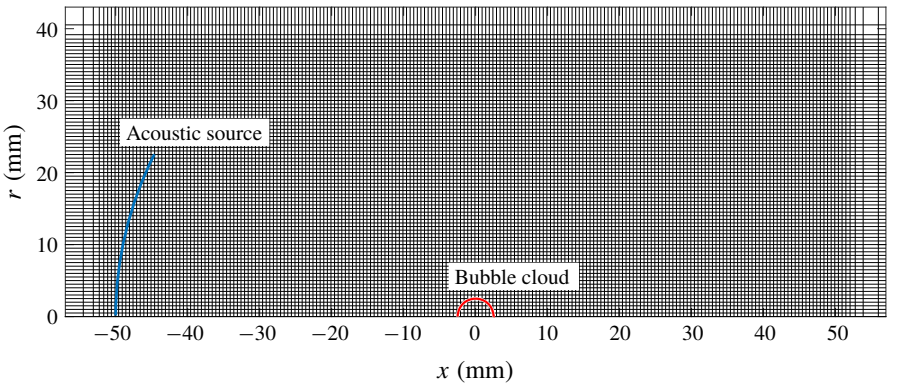


FIGURE 4. (Colour online) Schematic of the numerical set-up. Every fifth point is plotted in the computational mesh.

We will treat the first moment ($n = 1$), unless otherwise noted. The moments are normalized to vary within the range of $[-1, 1]$. In an extreme case, when monodisperse bubbles are distributed in a left hemisphere and oscillate with the same radial velocity, the first moments satisfy $\mu_{Vcn} = \mu_{Kcn} = -0.375$. Therefore, moments smaller than this value indicate a large bias in the volume or kinetic energy towards the proximal side of the cloud.

4. Cloud cavitation in a focused ultrasound wave

4.1. *Set-up*

In order to investigate the dynamics of bubble clouds, we conduct numerical simulations that mimic the laboratory set-up. Figure 4 shows a schematic of the numerical set-up. The size of the simulation domain is 500 mm × 250 mm, which has been verified to be sufficiently large to effectively mimic free space. For the initial condition, we randomly distribute bubble nuclei in a spherical region with radius 2.5 mm with its centre located at the origin of x–r axisymmetric coordinates. The grid size is uniform near the region of the bubble cloud with a characteristic grid size of 100 μm. Symmetry boundary condition is used on the axis of symmetry. The grid is smoothly stretched towards the other domain boundaries, where characteristic boundary conditions are used to reduce spurious reflections of waves. The transducer used in the experiment is modelled by an acoustic source uniformly distributed on a portion of spherical surface with an aperture of 30 mm and a radius of 50 mm concentric with the bubble cloud. The axis of the spherical surface is aligned with the axis of symmetry of the coordinates.

The modelled acoustic source is calibrated by comparing the focal pressure evolution with an experimental measurement with a low input voltage, producing the good agreement shown in figure 5. In the simulations of bubble clouds, the peak maximum and negative amplitudes are adjusted to 6.0 and −4.5 MPa, respectively. In the simulations, we excite pressure waves at the acoustic source surface with a frequency of 335 kHz, such that peak focal maximum and negative pressures without presence of bubbles are 6.0 and −4.5 MPa, respectively. This gives a root-mean-square pressure at the focal point of 1.8 MPa during $t \in [0, 50]$ μs. Details of the calibration are described in appendix A.

https://doi.org/10.1017/jfm.2018.968 Published online by Cambridge University Press

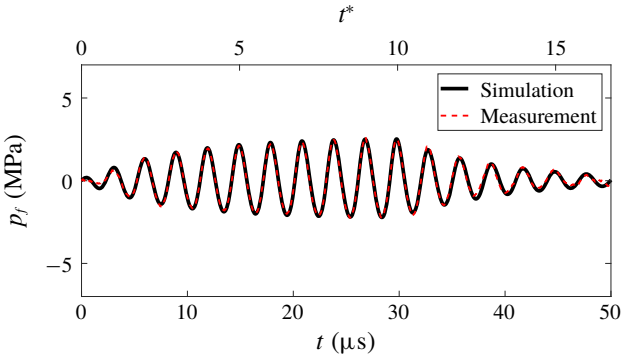


FIGURE 5. (Colour online) Focal pressure evolution of the modelled transducer and that of the experimental measurement. Parameter t^* denotes non-dimensional time, where $t^* = tf$.

Run	B_0	σ
F1	0.625	0
F2	1.25	0
F3	2.5	0
F4	5.0	0
F5	0.625	0.7
F6	1.25	0.7
F7	2.5	0.7
F8	5.0	0.7

TABLE 1. List of parameters used in the eight runs for simulations of bubble cloud dynamics in the focused ultrasound wave.

The parameters of bubble clouds used in the simulations are summarized in table 1. It is challenging to measure the population and the initial size distribution of nuclei in the experiment. Therefore, we empirically assess the effects of the nuclei population on the resulting bubble cloud dynamics by varying the value of B_0 within a range of $B_0 \in [0.625, 5]$. To assess the effect of polydispersity, for each value of B_0 we simulate monodisperse and polydisperse clouds. For the polydisperse case, the initial radii of bubbles follow a log-normal distribution given as $\ln(R_{b0}/R_{b,ref}) \sim N(0, \sigma^2)$ (Ando, Colonius & Brennen 2011), where $R_{b,ref}$ is the most probable bubble size, chosen as $R_{b,ref} = 10$ μm. In the monodisperse and polydisperse cases, we use $\sigma = 0$ and 0.7, respectively. Here, $\sigma = 0.7$ models highly polydisperse bubble clouds. This is in order to obtain an upper bound of the variability in the resulting bubble dynamics due to polydispersity. We neglect fission/break-up of bubbles during the simulations. In order to assess the variability of the bubble cloud dynamics due to the initial reference radius of bubbles, we also simulated monodisperse and polydisperse clouds with $R_{b0,ref} = 5$ μm with various values of B_0: $B_0 \in [0.625, 5]$. The results did not show a significant difference from cases with $R_{b0,ref} = 10$ μm, and thus they are omitted in this paper.

https://doi.org/10.1017/jfm.2018.968 Published online by Cambridge University Press

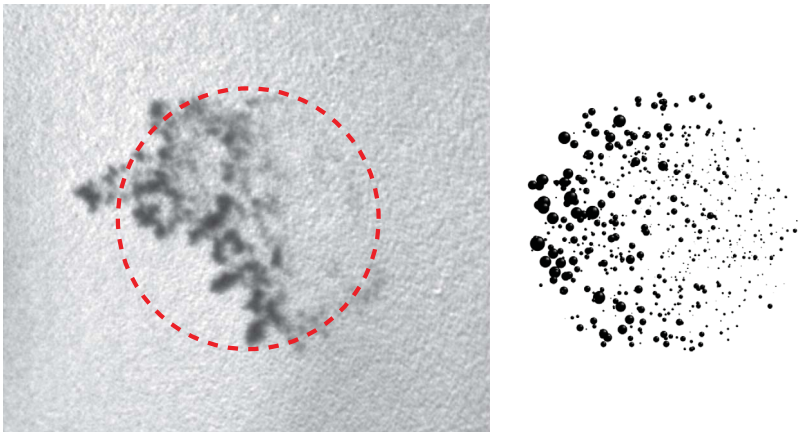


FIGURE 6. (Colour online) Images of the bubble cloud obtained in the experiment and simulation (run F7) at $t^* = 13.6$. The red dashed circle has a radius of 2.5 mm.

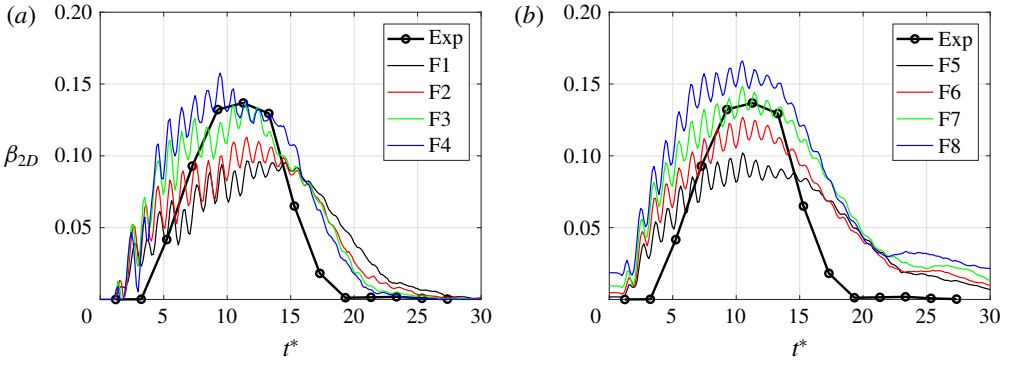


FIGURE 7. (Colour online) Comparisons of the evolutions of the two-dimensional void fraction of bubbles, defined in (4.1), during the experiment and the simulations with (*a*) monodisperse (runs F1–F4) and (*b*) polydisperse (runs F5–F8) clouds.

4.2. *Comparisons with the high-speed image*

Figure 6 compares the high-speed image (the seventh image of figure 1) and the image of bubbles obtained in run F7 at $t^* = 13.6$. A similar anisotropic structure is evident in the simulated cloud; the proximal bubbles are larger than the distal bubbles.

Figures 7(*a*) and 7(*b*) compare the evolutions of the two-dimensional void fraction of bubbles in the experiment and the simulation of initially monodisperse and polydisperse clouds, respectively. The two-dimensional void fraction is obtained as

$$\beta_{2D} = \frac{A_B}{\pi R_c^2}, \tag{4.1}$$

where A_B is the area occupied by the bubbles in the two-dimensional images. In all cases, the projected area steadily grows and reaches its maximum value within the range of 0.1–0.15 at around $t^* = 10$–15 then decays. Overall, trends in the evolution of the void fraction are similar between the monodisperse and polydisperse

https://doi.org/10.1017/jfm.2018.968 Published online by Cambridge University Press

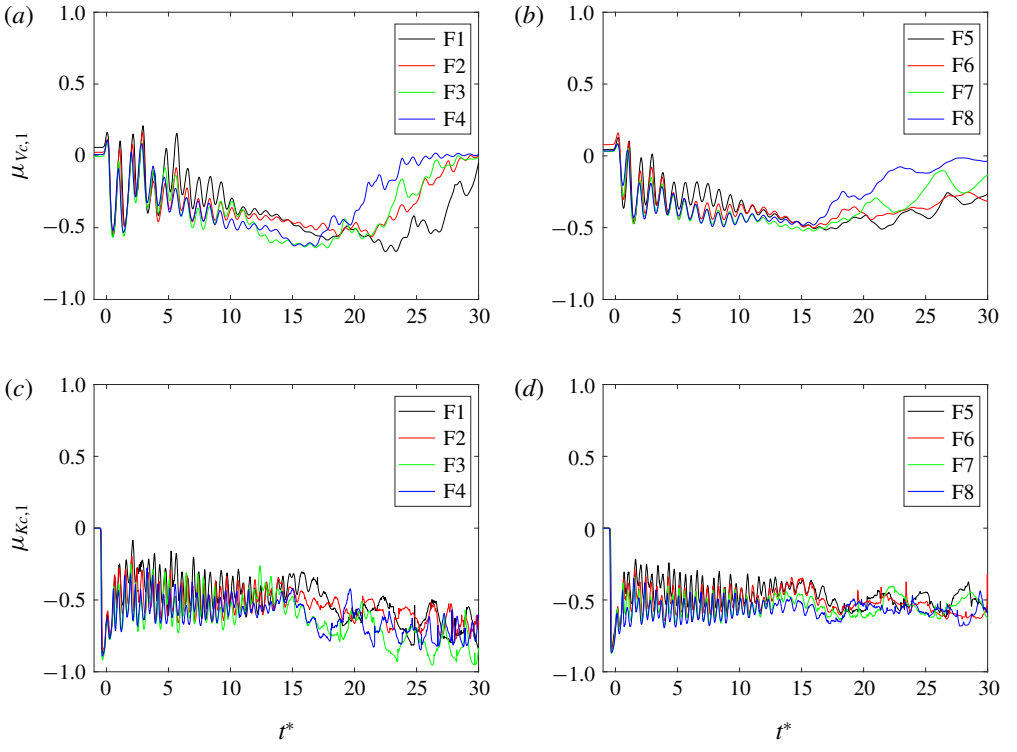


FIGURE 8. (Colour online) Evolution of (*a*,*b*) the moment of volume, $\mu_{Vc,1}$, and (*c*,*d*) the kinetic energy, $\mu_{Kc,1}$, of the simulated clouds. Results of (*a*,*c*) monodisperse (runs F1–F4) and (*b*,*d*) polydisperse (runs F5–F8) clouds are shown.

clouds, though the polydisperse clouds present slightly higher peak values than the monodisperse clouds with the same values of B_0. The magnitudes of the slope of the void fraction during the growth and the decay are larger in the experiment than the simulation. The discrepancies could be due to experimental uncertainties, including the size distribution of nuclei in the simulation, non-sphericity of the cloud in the experiment and the finite resolution and/or the noise of the high-speed images. Nevertheless, the results confirm that the simulated bubble clouds quantitatively reproduce the experimental observation with reasonable accuracy.

For quantification of the anisotropic structure, we compute evolutions of the moments of volume and kinetic energy in each cloud during the course of simulations. Figure 8 shows the result. In all clouds, the moment of volume oscillates around -0.25 during the passage of the wave until around $t^* = 17$ then grows back to zero. This suggests that the sizes of the proximal bubbles are larger than those of the distal bubbles for all t^* and the structural anisotropy is the most significant at around $t^* = 17$. After the initial transient, the moment of kinetic energy oscillates between -0.25 and -0.5 for all t^*. This indicates that the proximal bubbles experience a larger amplitude of pressure excitation and oscillate more actively than the proximal bubbles.

The results above indicate that the bubble dynamics is relatively insensitive to both the population and initial polydispersity of the clouds. Therefore, the anisotropic

https://doi.org/10.1017/jfm.2018.968 Published online by Cambridge University Press

Run*	A
A1v[1-4]	$10^{-1.5}$
A2v[1-4]	$10^{-1.0}$
A3v[1-4]	$10^{-0.5}$
A4v[1-4]	1
A5v[1-4]	$10^{0.5}$
A6v[1-4]	10

TABLE 2. List of parameters used in the parametric study. The numbering of 1 to 4 after the symbol v denotes values of nuclei densities, corresponding to distinct values of B_0: $B_0 = [0.625, 1.25, 2.5, 5.0]$, respectively. For each set of (A, B_0), five bubble clouds with distinct initial coordinates of bubbles are simulated.

*Anv[1–4] denotes Anv1, Anv2, Anv3 and Anv4, where $n = 1, 2, \ldots, 6$.

structure is expected to be observed over a wide range of the nuclei distribution and population.

5. Parametric simulations using plane ultrasound waves

5.1. *Set-up*

In the set-up considered in the previous section, bubbles are forced by the pressure wave with a complex waveform generated by a specific transducer. This hinders further generalization of the obtained results, including the anisotropic structure and the bubble-induced kinetic energy, to the bubble cloud dynamics excited in other geometries of pressure fields. For generalization, analysis using a wider range of parameters, but with a simpler geometry of acoustic source, is desirable. To this end, as an idealized problem, we conduct parametric simulations of bubble cloud dynamics excited by plane ultrasound waves of various amplitudes.

The set of parameters addressed in the simulations is summarized in table 2. The radius of clouds and variations of B_0 follow those of the previous section. It is realistic to assume that the radial distribution of bubbles is polydisperse rather than monodisperse in practical conditions. Thus we assume that the distribution of the initial radius of nuclei follows a log-normal distribution with $R_{b0,ref} = 10$ μm and $\sigma = 0.7$, but we expect only small differences from monodisperse clouds in the present cases.

The mesh size follows that of the previous section. We excite 10 cycles of a plane, sinusoidal pressure wave from a source plane located at $x = -20$ mm to the positive x direction, which gives the pressure at the origin, without bubble cloud, of

$$p_a = p_0[1 + H(10 - t^*)A\sin(2\pi t^*)], \tag{5.1}$$

where H is the Heaviside step function. The frequency of the wave is $f = 300$ Hz, and thus the wavelength is 4.9 mm and approximately equal to the diameter of the bubble clouds. In order to assess the variability of the bubble cloud dynamics due to spatial distribution of bubbles, with each set of (A, B_0) we simulate $N_s = 5$ clouds with distinct, random spatial distributions of nuclei. In the highest amplitude case with $A = 10$, the root-mean-square pressure without bubble during the period of excitation is 0.72 MPa. This pressure is of the same order of magnitude as that of the focused wave considered in the previous section. In what follows, we denote quantities obtained by

https://doi.org/10.1017/jfm.2018.968 Published online by Cambridge University Press

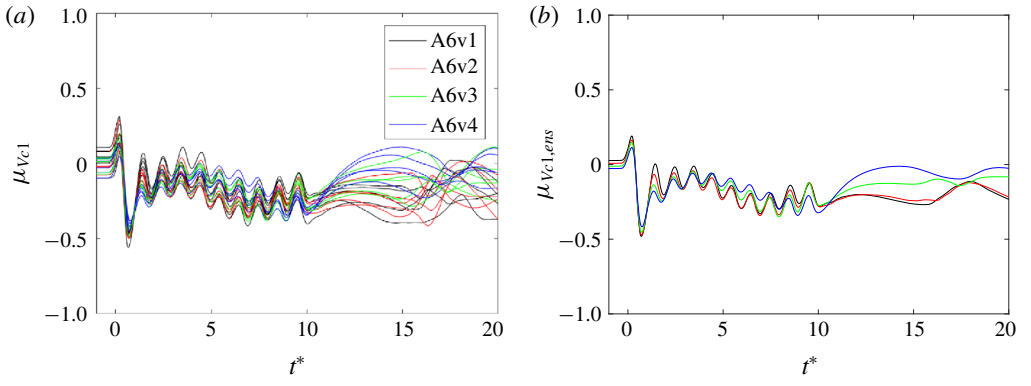


FIGURE 9. (Colour online) Evolution of the moment of volume of (*a*) all clouds and (*b*) ensemble-averaged clouds with $A = 10$ and various values of B_0 from runs A6v[1–4].

averaging N_s bubble clouds with the same set of (A, B_0) as those of ensemble-averaged cloud. We denote the ensemble average of arbitrary quantity f as

$$f_{ens} = \frac{1}{N_s} \sum_{i=1}^{N_s} f_i, \tag{5.2}$$

where f_i is obtained from the ith realization of the bubble cloud. In the present simulations, $N_s = 5$ is sufficient to obtain ensemble-averaged quantities.

5.2. *Anisotropic structure*

Here we analyse the volumetric evolution and the anisotropic structure of the clouds. We begin by looking at the highest amplitude case, $A = 10$, in detail.

Figure 9(*a*) shows evolutions of the moment of volume of bubble clouds from run A6v during the course of simulation. The moment of volume oscillates between -0.3 and 0 for all values of B_0 after initial transient until $t^* = 10$. After $t^* = 10$, the range of moment takes on a wider spread in values. In order to assess variability associated with the random position of bubbles, figure 9(*b*) shows the same quantities of the ensemble-averaged clouds. The similarity of the moments in the two plots indicates small incoherence among the the dynamics of bubble clouds of distinct realizations. The clouds share the same anisotropic structure regardless of the initial population and spatial distribution of nuclei.

Figure 10 shows images of bubble clouds at $t^* = 5.7$, obtained from one of the realizations from runs A6v[1–4]. As expected, the anisotropic structure is similar to that of the clouds excited by HIFU.

We now consider the effect of varying the excitation amplitude, A. In order to simplify the discussion, we concentrate on the dynamics during the excitation phase where $2 < t^* < 9$, and time-average (denoted by $\overline{(\cdot)}$) the corresponding moments. Figure 11 shows the time-averaged moment of volume plotted against the normalized amplitude of the incident wave. Regardless of B_0, the moment of volume is small and nearly constant with A up to around $A = 1$. For $A > 1$ the moment decreases, indicating larger anisotropy. Thus anisotropy is observed with high-amplitude excitation.

To understand this dependency of the structure on the pressure amplitude, we use the Keller–Miksis equation to examine the nonlinear response of a single, isolated

https://doi.org/10.1017/jfm.2018.968 Published online by Cambridge University Press

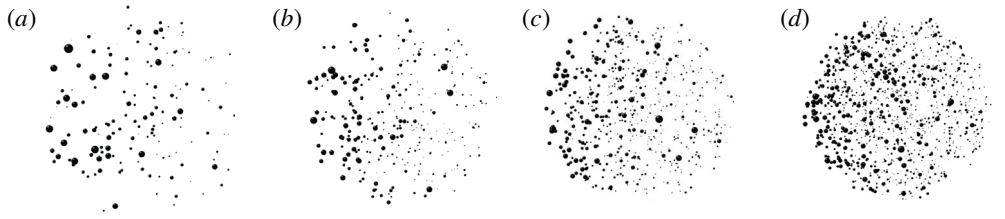


FIGURE 10. Images of the bubble clouds with $A = 10$ and various values of B_0 at $t^* = 5.7$ from runs (*a*) A6v1, (*b*) A6v2, (*c*) A6v3 and (*d*) A6v4.

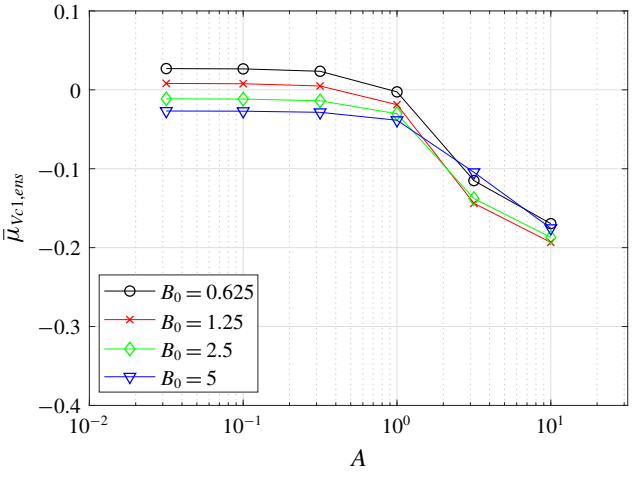


FIGURE 11. (Colour online) Time-averaged moment of volume of all the ensemble-averaged clouds against the normalized amplitude of the incident wave.

spherical bubble with an initial diameter of 10 μm under periodic far-field pressure excitation with a frequency of 300 kHz. Figure 12(*a*) shows a bifurcation diagram of the radius of the bubble sampled at every period of forcing pressure with a slowly increasing forcing amplitude within the range addressed in the parametric study. The computed radius monotonically grows with A and experiences a sub-harmonic bifurcation at $A \approx 1.65$, then transits to a chaotic regime with a growing amplitude of radius. The bifurcation diagram in this range of the excitation amplitude was also reported by Preston *et al.* (2007). At $A \approx 2.85$, the radius returns to a quasi-periodic behaviour, then at $A \approx 4$ it re-transits to a chaotic regime with an amplitude growing with A.

Figure 12(*b*) shows the time-averaged volume of the same bubble during the period of forcing. The growth of the averaged volume follows a similar trend to that of the radius, but with a larger slope. The volume smoothly grows to $\overline{V}_b/V_{b0} \approx 5$ with A then discontinuously grows to $\overline{V}_b/V_{b0} \approx 12$ at $A \approx 2.85$. Then it grows with much faster rate with A, towards $\overline{V}_b/V_{b0} \approx 50$ at $A = 10$. The nonlinear growth of the volume with $A > 1$ corresponds to cavitation.

Figure 13(*a*) shows the evolution of the moment of kinetic energy of clouds A6v. After the initial transient until $t^* = 10$, the moments of kinetic energy oscillate between -0.5 and 0 around an approximately constant level, after which oscillations with larger amplitudes occur. Figure 13(*b*) shows the same quantities of

https://doi.org/10.1017/jfm.2018.968 Published online by Cambridge University Press

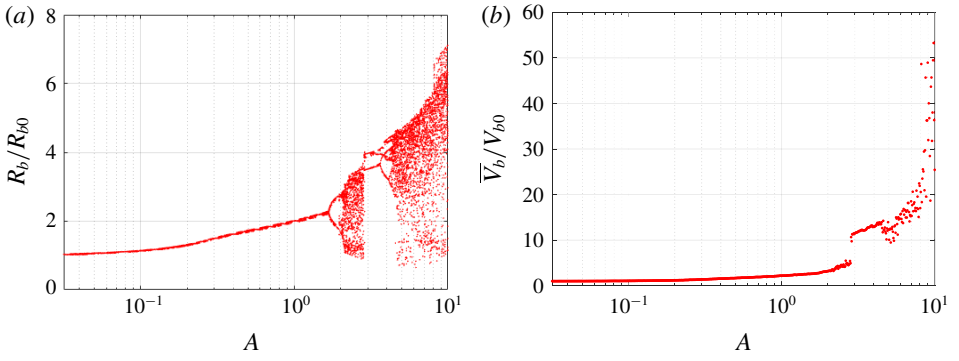


FIGURE 12. (Colour online) (*a*) Bifurcation diagram of the bubble radius and (*b*) averaged volume of a single, spherical bubble under periodic pressure excitation with varying amplitude.

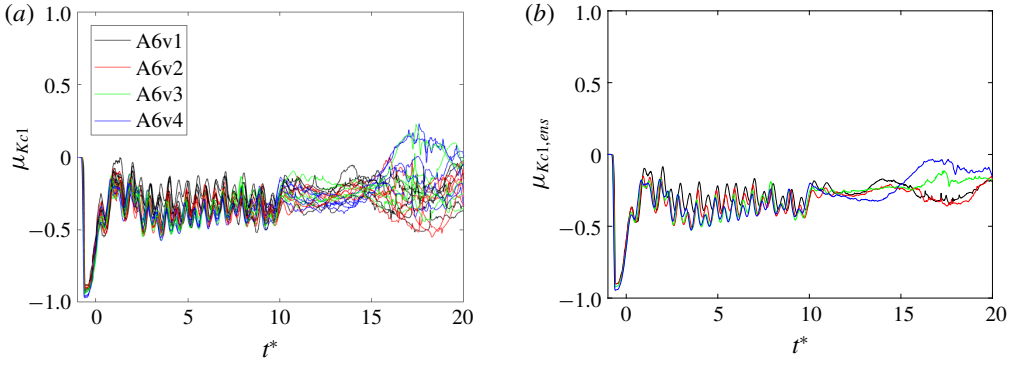


FIGURE 13. (Colour online) Evolution of the moment of kinetic energy of (*a*) all clouds and (*b*) ensemble-averaged clouds with $A = 10$ and various values of B_0 from runs A6v[1–4].

the ensemble-averaged clouds. The result is similar to that of figure 13(*a*), further confirming that the trend of the moment results from the coherent dynamics of the cloud. The plots indicate that the oscillations of proximal bubbles are more energetic than the distal bubbles during the course of excitation, regardless of the initial nuclei population. Since the moment of volume and the moment of kinetic energy reach quasi-stationary states during the 10 cycles of pressure excitation, increasing the number of cycles of the pressure excitation may not largely affect the structure of the clouds. When the number of cycles is as small as 1, however, the bubble dynamics does not reach the stationary state, as shown in $t^* \in [0, 1]$ in figure 13, and the structure may not be observed.

The results of single bubble dynamics in figure 12 and the moment of energy in figure 13 may explain the mechanism of the anisotropic structure. The bubbles nearest the source are exposed to an incoming pressure wave, while the distal bubbles experience smaller amplitudes of pressure fluctuations due to the scattering of the wave by the proximal bubbles. This results in larger amplitude of oscillations of bubbles locally in the region near the proximal surface of the cloud, seen as the bias in the moment of kinetic energy. With a pressure amplitude larger than $A > 1$, the

https://doi.org/10.1017/jfm.2018.968 Published online by Cambridge University Press

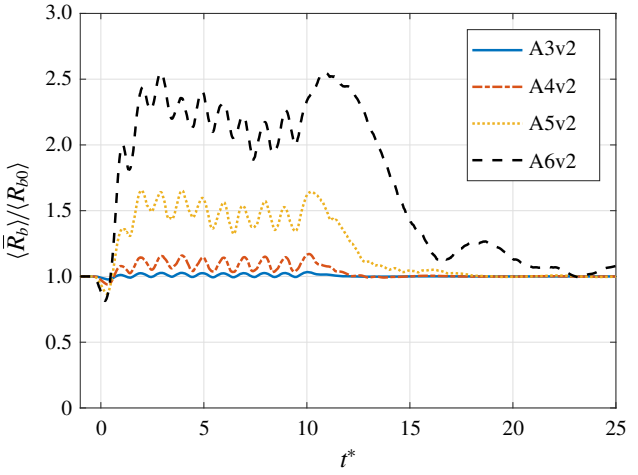


FIGURE 14. (Colour online) Evolution of the mean radius of bubbles in ensemble-averaged clouds with $B_0 = 1.25$ and various values of A from runs A[3–6]v2.

proximal bubbles can grow to much larger radius than the distal bubbles due to local cavitation, which results in the bias in the centre of volume, and becomes visible as the anisotropic structure.

The evolutions of the moments of kinetic energy in figure 8(*c*,*d*) and those in figure 13(*a*,*b*) are similar during the period of ultrasound excitation; they oscillate around 0.4. This indicates that the clouds excited by the focused and plane waves present similar dynamical features including structural anisotropy, and confirms that the parametric study using the plane wave can represent the dynamics of the bubble cloud excited by the focused wave.

5.3. *Dynamic cloud interaction parameter*

In order to further quantify the bubble cloud dynamics, we seek to generalize the definition of the cloud interaction parameter introduced by DB. The critical difference in the bubble cloud dynamics in the present study and that considered by DB lies in the wavelength and the amplitude of the pressure excitation. As discussed in § 3, the original interaction parameter can be interpreted as a scaling parameter of the global kinetic energy of liquid induced by small-amplitude oscillations of a bubble cluster under weak pressure excitation with long wavelength. Meanwhile, in the bubble clouds considered in the present study, the wavelength is as small as the size of a cloud. Due to the strong amplitude of the pressure, bubbles experience cavitation growth and their radii can deviate from their initial values. The radius of bubbles can also vary in space.

Figure 14 shows the evolutions of the spatial mean of the radius of bubbles in the cloud with $B_0 = 1.25$, normalized by its initial value, with various values of the excitation amplitude: $A = [10^{-0.5}, 1.0, 10^{0.5}, 10]$. For $A > 1$, the mean radius grows rapidly on arrival of the wave, then oscillates around an approximately constant value larger than 1 until $t^* = 10$, while for $A < 1$ the mean radius oscillates around 1. After $t^* > 10$ the radius decays to the initial value in all cases. This indicates that the spatial mean of the bubble radius oscillates around the quasi-stationary equilibrium whose value is unique to the pressure amplitude during the course of excitation.

https://doi.org/10.1017/jfm.2018.968 Published online by Cambridge University Press

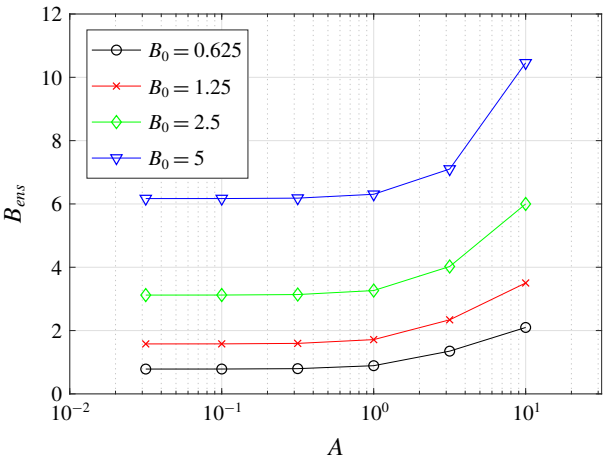


FIGURE 15. (Colour online) Dynamic interaction parameter of all the ensemble-averaged clouds plotted against the amplitude of pressure excitation.

Motivated by this result, we extend the definition of the cloud interaction parameter as

$$B = \frac{N_b \langle \overline{R}_b \rangle}{R_{c,L}}, \tag{5.3}$$

where $\overline{R}_b$ is the time-averaged radius of the bubble during the pressure excitation. Hereafter we denote this parameter as dynamic cloud interaction parameter. A detailed discussion motivating the specific form of B is given in appendix C.

In figure 15, we plot the average value of B (over the ensemble) obtained for all the runs in table 1. For all the values of B_0, B monotonically grows and deviates from B_0 for $A > 1$. This is due to deviation of $\langle \overline{R}_b \rangle$ from $R_{b,ref}$ and thus can be associated with the cavitation growth of the mean bubble radius in the cloud shown in figure 15 with $A > 1$.

5.4. *Scaling of the moment of kinetic energy*

The dynamic interaction parameter is proposed as an appropriate scaling parameter for bubble cloud dynamics excited in the short-wavelength regime. In this section, to examine the extent to which B controls the dynamics, we correlate the moment of kinetic energy against both B and the original cloud interaction parameter, B_0, and compare the results.

Figures 16(*a*) and 16(*b*) show scatter plots of the time-averaged, first and third moments of kinetic energy against B_0 and B, respectively. The first and third moments show negative correlations against both B_0 and B, while the data points are vertically more spread against B_0 than against B. The dynamic parameter does a somewhat better job of collapsing the dynamics than the original one. However, once we ensemble-average the data in figure 16(*c*,*d*), we see that much of the variation is associated with the randomized positions of the bubbles, and, in general, the dynamic interaction parameter collapses the moment of kinetic energy of the clouds. This confirms that the moments of kinetic energy can been seen as monotonic, decreasing functions of B. Overall, the results indicate that B is a more appropriate parameter to scale the

https://doi.org/10.1017/jfm.2018.968 Published online by Cambridge University Press

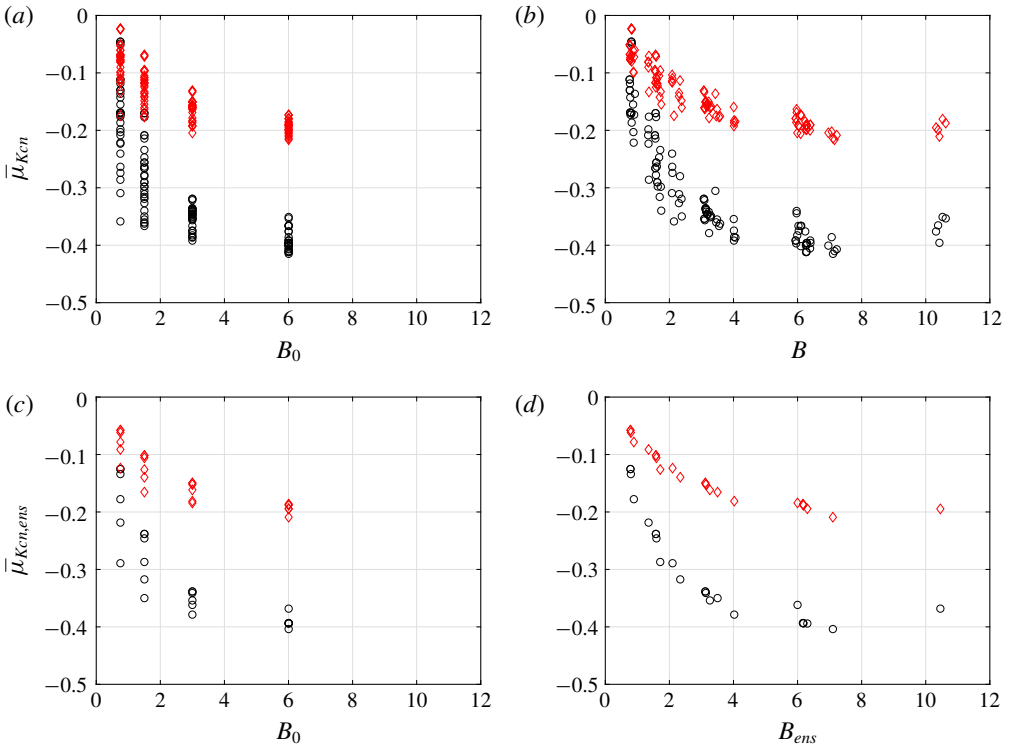


FIGURE 16. (Colour online) Scatter plots of the time-averaged moments of kinetic energy against B_0 and B. (*a*,*b*) All realizations; (*c*,*d*) the ensemble-averaged values. Circle and diamond denote the first and third moments, respectively.

moments than B_0. The similarity of figures 16(*b*) and 16(*d*) indicates small variability of the spatial bias in the energy due to initial spatial distribution of bubbles.

The moments in figure 16(*d*) approach zero for small B, which confirms that in the limit of $B = 0$ inter-bubble interactions are negligible and the resulting spatial bias in the mean kinetic energy is statistically zero, since bubbles experience the same amplitude of pressure excitation at any location in the cloud. The plots also indicate that as B increases, the slope of the curve monotonically decreases and thus the moment saturates. This indicates that the distribution of energetic bubbles in the cloud becomes more localized in the proximal side of the cloud with increasing pressure amplitude, while the magnitude of energy localization eventually becomes invariant to the amplitude.

Overall, the results of the parametric simulation further elucidate the underlying mechanism of the anisotropic structure. When the inter-bubble interaction becomes dominant, energy localization occurs for the cloud, and this happens regardless of the amplitude of pressure excitation. Meanwhile, the anisotropic structure becomes visible only when the energetic, proximal bubbles cavitate and reach a large radius that is a nonlinear function of the amplitude of pressure excitation. It is notable that, in fact, the moment of volume is not collapsed by the dynamic cloud interaction parameter. Figure 17 shows scatter plots of the time-averaged moment of volume against the dynamic cloud interaction parameter. For the entire range of B, the moment is scattered between -0.3 and 0.1 for all realizations and the ensemble-averaged values.

https://doi.org/10.1017/jfm.2018.968 Published online by Cambridge University Press

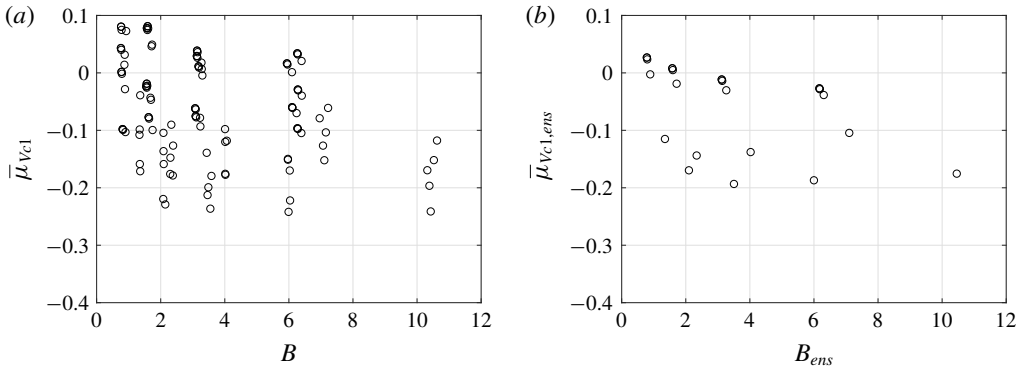


FIGURE 17. Scatter plots of the time-averaged moments of volume against B. (a) All realizations; (b) the ensemble-averaged values.

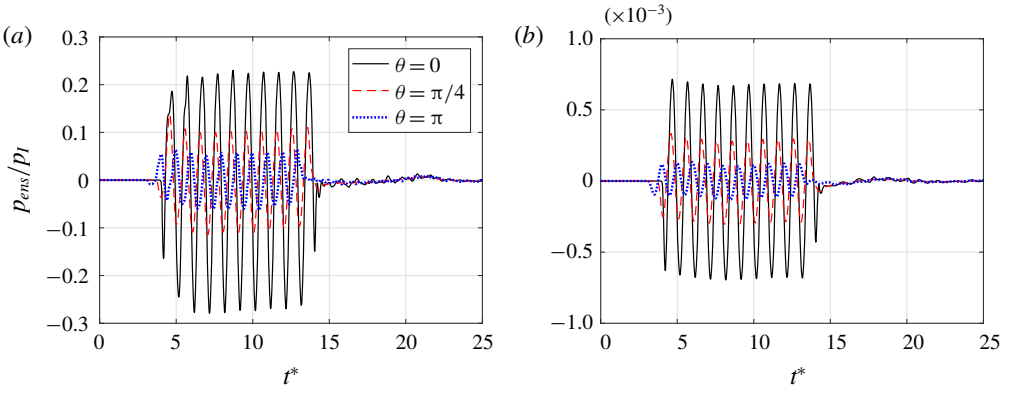


FIGURE 18. (Colour online) Evolution of the scattered pressure field at a distance $r = 8R_c$ from ensemble-averaged clouds from runs (a) A6v4 and (b) A1v1.

5.5. *Scaling of the far-field, bubble-scattered acoustics*

Given the successful scaling of the moments of kinetic energy in terms of the dynamic interaction parameter, we are motivated to explore scaling of the far-field, bubble-scattered acoustics that result from the bubble cloud dynamics.

Figure 18 shows the evolution of the far-field sound at different angles to the direction of incident radiation. The pressure has been normalized by the amplitude of the incident wave. These are plotted for two cases: figure 18(a) shows the densest cloud excited by the highest amplitude wave (thus obtaining the largest value of B), while figure 18(b) shows the most dilute cloud with the lowest amplitude of excitation (lowest value of B). The scattered pressure shows sinusoidal oscillations at a retarded time associated with the incident wave scattered to the sampling location. The amplitude of the scattered pressure from the dense cloud is an order of magnitude larger than that from the dilute one for all t^*. The small, rapid fluctuations at large t^* are due to the bubble oscillations after the passage of the incident wave. The small amplitude of these fluctuations indicates the absence of a strong, coherent cloud collapse.

https://doi.org/10.1017/jfm.2018.968 Published online by Cambridge University Press

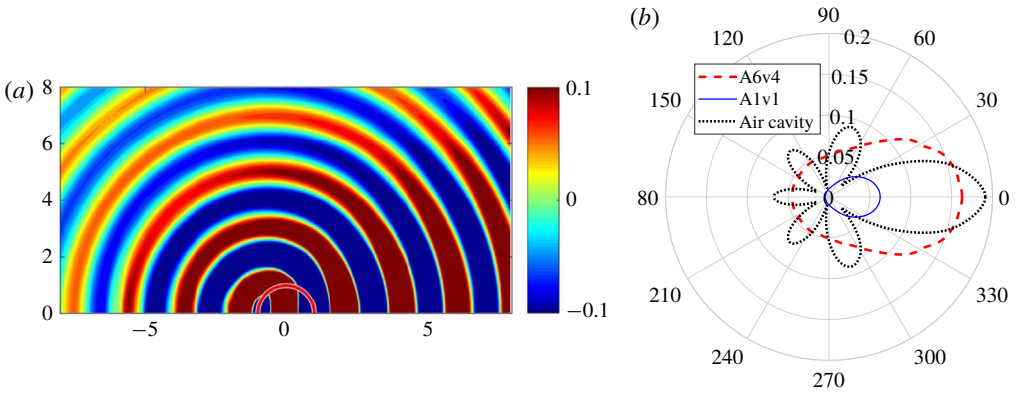


FIGURE 19. (Colour online) (*a*) Contours of the scattered pressure field at $t^* = 9.6$, normalized by the amplitude of the incident wave, obtained from run A6v4. The length unit is $R_c = 2.5$ mm. (*b*) Polar plots of the root-mean-square pressure sampled on spherical surface with $r/R_c = 8$. Results from runs A6v4 and A1v1 are compared to the scattering of a single spherical air bubble of the same size as the cloud.

Figure 19(*a*) shows a contour plot of the bubble-scattered component of the pressure field at $t^* = 9.6$ from the dense cloud. The scattered component is obtained by subtracting the contribution of the incident pressure wave from the total pressure field. The scattered wave propagates radially outward from the bubble cloud. Figure 19(*b*) shows a polar plot of the scattered waves from both clouds averaged over the period of direct scattering. The linear scattering from a single spherical air cavity with the same radius as the clouds is also shown for reference. With both clouds, scattering is dominant over angles in the forward direction. The amplitude of scattering is larger at all angles from the dense cloud than from the dilute one.

Figure 20 is the analogue to figure 16 but with the root-mean-square pressure plotted versus the original and dynamic cloud interaction parameters. Shown by the different colours are the three scattering angles considered in figure 18. The scattered pressure shows positive correlations with both B_0 and B. The data points are widely spread against B_0, but collapse better with B. As was the case with the kinetic energy moment, ensemble averaging of the clouds removes additional scatter associated with the randomized bubble positions and distribution. Overall, the results confirm that the proposed interaction parameter scales the amplitude of the bubble-scattered acoustics better than the original parameter.

The polar plots shown in figure 19 may help explain the saturation of both the moments of kinetic energy and the amplitude of bubble-scattered acoustics with a large value of the dynamic interaction parameter. Due to the large mismatch in the acoustic impedance across the air–water interface, a cavity can scatter the most portion of the incident wave energy. The dense cloud gives a similar magnitude of scattering as a single large bubble. A subsequent increase in either the excitation amplitude or cloud volume fraction (thus increasing B) yields no further effect; the scattered acoustics saturate at a level similar to a single bubble of the cloud dimension. The smaller directionality of the scattered acoustics by the cloud than by the air cavity is associated with the spatially random distributions of bubbles. In multiple scattering theory, scatterers with a random, disordered distribution may act as a rough surface and result in randomized angles of scattering of the incoming wave, compared to a smooth surface like that of the air cavity (Ishimaru 1978).

https://doi.org/10.1017/jfm.2018.968 Published online by Cambridge University Press

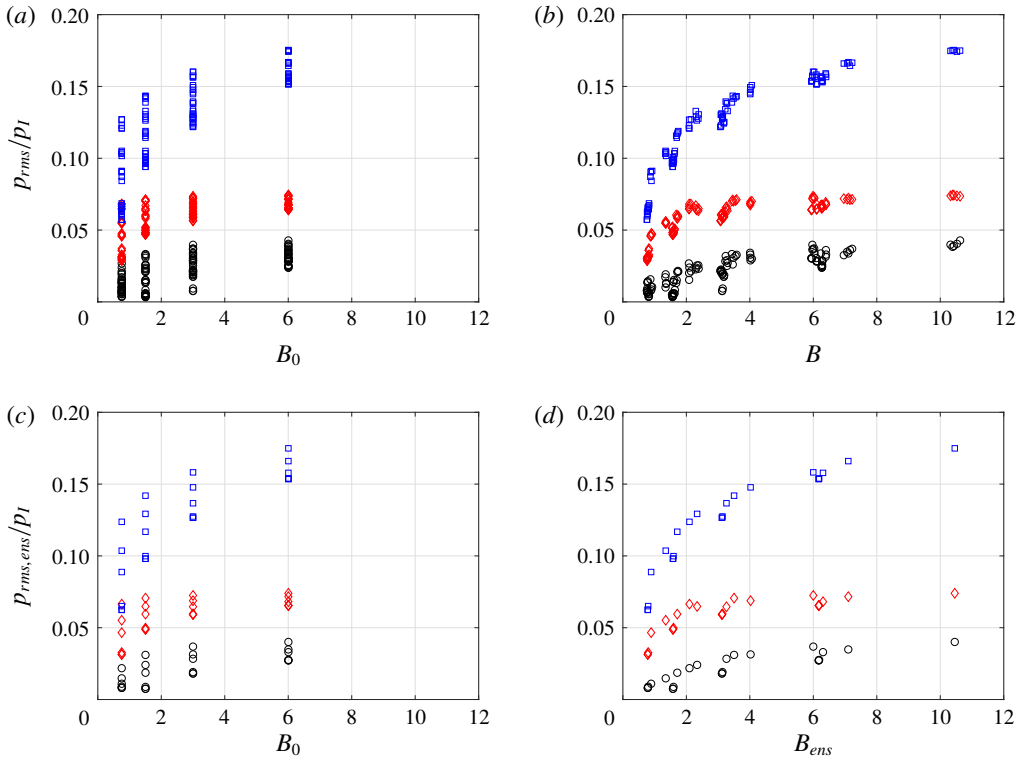


FIGURE 20. (Colour online) Scatter plots of the root-mean-square pressure against B_0 and B. (*a*,*b*) All realizations; (*c*,*d*) the ensemble-averaged values.

Overall, it has been shown that the dynamic interaction parameter scales both the amplitude of the scattered acoustic field as well as the moment of kinetic energy. Furthermore, this indicates direct correlations between the far-field acoustics and the moment. Figures 21(*a*) and 21(*b*) show data for all clouds considered at the three observer angles, with and without ensemble averaging, respectively. For applications, the result indicates that the measurement of the far-field, bubble-scattered pressure waves can be used as a surrogate for the magnitude of the energy localization in the bubble cloud as well as a means to estimate the value of B.

6. Implications for cavitation in lithotripsy

As the central application and motivation of the present study, it is worth discussing implications of the present results of numerical experiments for HIFU-based lithotripsy.

In ESWL, bubbles in a cloud experience a nearly identical amplitude of pressure excitation during the passage of the tensile component of the wave since the tensile tail typically has a much larger width than the cloud size. The dynamics of bubble cloud consists of spherically symmetric structures, similar to that shown in figure 2. The inward-propagating shock wave causes violent cloud collapse, which results in erosion of surrounding materials. This injurious effect has been seen as a major disadvantage of ESWL (McAteer *et al.* 2005; Bailey *et al.* 2006).

https://doi.org/10.1017/jfm.2018.968 Published online by Cambridge University Press

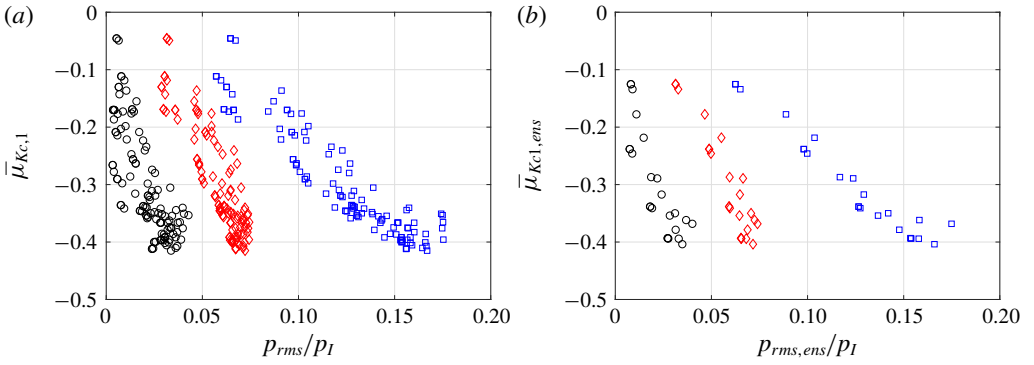


FIGURE 21. (Colour online) Scatter plots of the moments of kinetic energy against p_{rms} for (*a*) all clouds and (*b*) ensemble-averaged clouds.

The use of HIFU for lithotripsy has been proposed as an alternative to ESWL due to the potentials for safer and more efficient stone comminution (Ikeda *et al.* 2006; Yoshizawa *et al.* 2009; Maxwell *et al.* 2015). Cavitation bubble clouds in HIFU-based lithoripsy, by contrast to those in ESWL, have a cloud size commensurate with the ultrasound wavelength. The resulting energy localization of the cloud and scattering of the incoming waves identified in the previous sections indicate that the bubble clouds with a size of the order of the incident pressure wavelength can result in strong scattering of the incident wave, with strong implications for HIFU-based lithotripsy.

Figure 22 compares contours of the maximum pressure on the cross-plane over the course of the simulations without bubble cloud, and with bubble clouds with $B_0 =$ 0.625 and 5.0. Without the bubble cloud, the region of high pressure (>5 MPa) is localized to the focal region of $x \in [-10, 5]$ mm. With the bubble clouds, the region of high pressure does not penetrate into the cloud except near the proximal surface. This can be interpreted in that the energetic proximal bubbles scatter the incoming wave to prevent the wave from penetrating into the cloud and suppress excitation and oscillation of the distal bubbles. There exists energy shielding. The small values of the maximum pressure within the cloud shown in figure 22(*b*,*c*) also indicate that strong cloud collapse does not occur during or after passage of the wave. This agrees with the absence of strong acoustic signals from bubble clouds after the passage of an incident plane wave confirmed in the numerical experiment, shown in figure 15. The results are reminiscent of a bubble screen (Carstensen & Foldy 1947; Commander & Prosperetti 1989) that provides a similar shielding effect. Though the high-pressure region penetrates into the bubble cloud with $B_0 = 0.625$ (figure 22*b*) more than into the cloud with $B_0 = 5.0$ (figure 22*c*), the distributions of the maximum pressure outside the clouds are similar in the two cases. This similarity indicates that the energy shielding can be caused by bubble clouds with wide ranges of the nuclei population and the initial void fraction.

In practical conditions of HIFU-based lithotripsy, cavitation bubble clouds can be nucleated on the surface of a kidney stone. It can be conjectured that such bubble clouds may have both positive and negative effects on the outcomes of the therapy; they can be less injurious due to the absence of violent cloud collapse, but they could reduce the efficacy of stone comminution by scattering the incident radiation. Meanwhile, it is apparent that the presence of kidney stones may complicate the resulting bubble cloud dynamics. For instance, non-spherical bubble collapse may

https://doi.org/10.1017/jfm.2018.968 Published online by Cambridge University Press

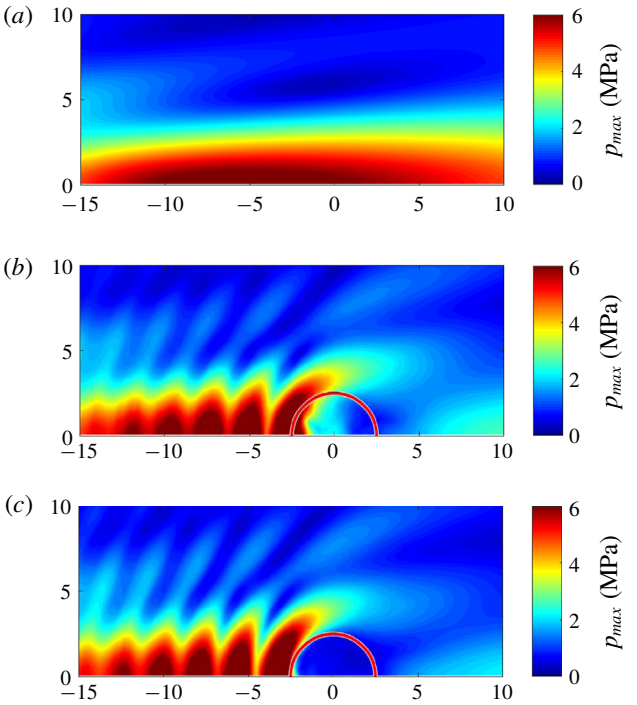


FIGURE 22. (Colour online) Contours of the maximum pressure over the course of the simulations (*a*) without, and with the bubble cloud from (*b*) run F5 and (*c*) run F8. The length unit is mm.

occur on the surface of a stone to cause erosion (Tomita & Shima 1986; Johnsen & Colonius 2009), an effect not considered in the present study. For future research, simulations of bubble cloud dynamics in the presence of a stone are desirable.

7. Conclusion

We investigated the dynamics of cavitation bubble clouds excited by strong ultrasound waves in a regime where the cloud size is similar to the ultrasound wavelength. In a first set of simulations, we excited bubble clouds by a focused ultrasound wave to mimic the laboratory set-up of HIFU-based lithotripsy. An anisotropic cloud structure was observed in both experiments and simulations. The proximal bubbles grow to a larger radius than the distal bubbles. In a second series of simulations, we elucidated the underlying mechanisms leading to the anisotropy of the observed structure and dynamics. In these simulations, we varied the amplitude of (plane-wave) excitation, the number density of bubbles, and we considered an ensemble of five runs for each case with different locations and populations of bubbles. Based on the kinetic energy of liquid induced by oscillations of a bubble cluster, we proposed a new scaling parameter, namely a dynamic cloud interaction parameter, that scales the observed anisotropy and dynamics. The parameter is generalized from the cloud interaction parameter introduced by d'Agostino & Brennen (1989) for linearized bubble cloud dynamics in the long-wavelength regime. We likewise showed that the scattered acoustic field collapses with the same dynamic interaction parameter, and thus can serve as a surrogate measure for the extent of energy localization in the

https://doi.org/10.1017/jfm.2018.968 Published online by Cambridge University Press

cloud. This correlation may be of use to diagnose *in situ*, via acoustic monitoring, the state of cavitation during ultrasound therapy as well as in various fluid flows that involve cloud cavitation phenomena.

Acknowledgements

The authors thank Adam Maxwell, Wayne Kreider and Michael Bailey for their support in the companion experiments. K.M. acknowledges the Funai Foundation for Information Technology, for the Overseas Scholarship. This work was supported by the National Institutes of Health under grant P01-DK043881 and ONR grant N00014-17-1-2676. The computations presented here utilized the Extreme Science and Engineering Discovery Environment, which is supported by the National Science Foundation, grant number CTS120005.

Appendix A. Experimental set-up

Here we describe the experimental set-up used to obtain images of the bubble cloud shown in figure 1. Figure 23(*a*) shows a schematic of the set-up. The set-up is designed to capture the evolution of a single, isolated cavitation bubble cloud excited in a focused, travelling ultrasound wave. The temperature and pressure are ambient. The water is degassed by a vacuum pump to realize an oxygen level of 75 %. A medical transducer composed of six piezo-ceramic array elements (figure 23*b*) is immersed in water. The transducer has an aperture of 110 mm $\times$ 104 mm, and a focal length of 120 mm. An imaging probe is attached at the centre of the transducer. We excite burst waves at the transducer with a pulse-repetition frequency of 200 Hz. A high-speed camera captures a rectangular region with dimensions of 15.3 mm $\times$ 12.5 mm around the focal point of the transducer. The camera captures 14 consecutive frames with a frame rate of 6 μs and an exposure time of 50 ns, with a resolution of 1200 $\times$ 980 pixels. A focused passive cavitation detector (PCD) with a poly(vinylidene difluoride) membrane, with receiver operating characteristic of 150 mm and an aperture of 50 mm, is positioned confocal to the transducer. We use acoustic signals captured by the imaging probe and the PCD to map the location of the cavitation site to confirm that the bubble cloud captured by the camera is isolated and no other cloud is present outside the window of the camera. Note that all the high-speed images presented in this paper are vertically reflected for consistency with the simulations.

Due to the stochastic nature of cavitation inception, it is challenging to nucleate a perfectly spherical, isolated, single bubble cloud in the experiment. The image of the bubble cloud shown in figure 1 is not perfectly circular, which represents the typical uncertainty in the shape of bubble clouds in the experiment. Nevertheless, even though their shapes are not perfectly circular/spherical, bubble clouds commonly possess right–left anisotropy, in that proximal bubbles grow to larger radius than distal bubbles.

With the input of N_c cycles of a sinusoidal voltage, the output of the transducer is modelled by the following formula:

$$p_{trans} = p_a \cos(2\pi f t)\left[(1-\mathrm{e}^{-t/\tau_u}) - (1-\mathrm{e}^{-(t-N_c/f)/\tau_d})H\left(t-\frac{N_c}{f}\right)\right], \qquad (A\,1)$$

where τ_u and τ_d are the ring-up and ring-down time, respectively. In the simulations of focused waves, we excite this expression of the pressure at the source plane, with

https://doi.org/10.1017/jfm.2018.968 Published online by Cambridge University Press

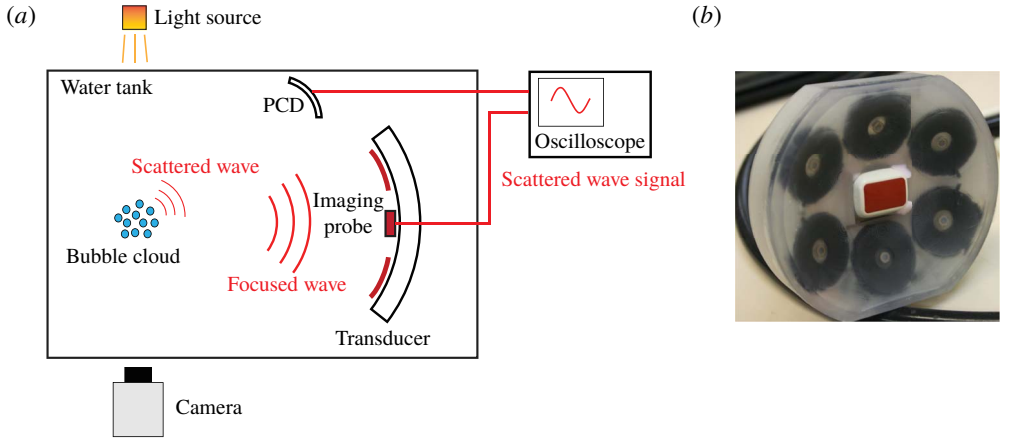


FIGURE 23. (Colour online) (*a*) Schematic of the experimental set-up. (*b*) Piezo-ceramic medical transducer used in the experiment.

$\tau_u = 4.0$ and $\tau_u = 8.0$ μs. The validity of acoustic source model is confirmed by comparing the focal pressure with experimental measurement as shown in figure 5. In the experiment, the focal pressure evolution was obtained in highly degassed water such that cavitation is suppressed (Canney *et al.* 2008).

Appendix B. Remark on the Keller–Miksis equation

Here we remark on the conservation equation of the bubble interior used to close the Keller–Miksis equation. By assuming that the pressure and the temperature of the gas–vapour mixture are uniform in the bubble, the conservation of energy of the gas can be reduced to (Prosperetti, Crum & Commander 1988)

$$\frac{\mathrm{d}p_{Bn}}{\mathrm{d}t} = \frac{-3\gamma_g}{R_n}\left[p_{Bn}\left(\dot{R}_n - \frac{J_V}{\rho_l}\right) + \frac{\gamma - 1}{\gamma}J_H\right], \tag{B 1}$$

$$\frac{\mathrm{d}m_{Vn}}{\mathrm{d}t} = 4\pi R_n^2 J_V, \tag{B 2}$$

where J_H and J_V are the heat and (vapour) mass flux across the bubble surface and m_{Vn} is the vapour mass in the bubble. Fluxes J_H and J_V are modelled using constant heat and mass transfer coefficients following Preston *et al.* (2007). Fluxes J_H and J_V are functions of m_v and defined by the thermodynamic property of the gas and the vapour. Overall, equations (2.11)–(2.12) and (B 1)–(B 2) represent a system of ordinary differential equations in terms of $[R_n, \dot{R}_n, p_{Bn}, m_{Vn}]$, which can be integrated given initial conditions and p_∞.

Appendix C. Local cloud interaction parameter

Here we provide a rationale for defining the dynamic cloud interaction parameter. To treat a bubble cloud in which bubbles experience non-uniform forcing pressure due to the short wavelength, we introduce the notion of local kinetic energy. The local energy is defined as the kinetic energy of liquid induced by bubbles in a spherical

https://doi.org/10.1017/jfm.2018.968 Published online by Cambridge University Press

region around a coordinate $\boldsymbol{x}$ with a radius of $R_{c,L}$ that experiences approximately uniform pressure excitation, namely local cloud:

$$K_{Local}(\boldsymbol{x}) = 2\pi\rho_l \left[\sum_{i}^{N_{b,L}} R_i^3 \dot{R}_i^2 + \sum_{i}^{N_{b,L}} \sum_{j}^{N_{b,L}} \frac{R_i^2 R_j^2 \dot{R}_i \dot{R}_j}{r_{i,j}} + O\left(\frac{R^7 \dot{R}^2}{r^4}\right) \right] \tag{C 1}$$

$$\sim \rho_l N_{b,L} R_L^3(\boldsymbol{x}) \dot{R}_L^2(\boldsymbol{x}) \left(1 + \frac{N_{b,L} R_L}{R_{c,L}}\right). \tag{C 2}$$

As discussed in § 3, with a strong pressure excitation, the mean bubble radius can largely deviate from its initial value. In the case of periodic pressure excitation, a natural choice of R_L can be its time-averaged value during the course of excitation:

$$R_L \approx \overline{R}_{b,L}. \tag{C 3}$$

This leads us to define the following *local* cloud interaction parameter:

$$B_L(\boldsymbol{x}) \approx \frac{N_{b,L} \overline{R}_{b,L}(\boldsymbol{x})}{R_{c,L}}. \tag{C 4}$$

The local interaction parameter characterizes the kinetic energy of the local cloud. We take a summation of this parameter over all the local clouds:

$$\sum_{i=1}^{N_c} B_L(\boldsymbol{x}) = N_c \langle B_L \rangle = \frac{N_b \langle \overline{R}_b \rangle}{R_{c,L}}, \tag{C 5}$$

where $\langle \cdot \rangle$ denotes the spatial average over the global bubble cloud. By multiplying a factor $R_{c,L}/R_c$, we obtain

$$\frac{N_c R_{c,L}}{R_c} \langle B_L \rangle = B. \tag{C 6}$$

The relation indicates that if the spatial distributions of B_L in distinct clouds are identical, the clouds also possess the same B and show a similar dynamic response. Conversely, if distinct clouds possess the same value of B, we could expect a similar spatial distribution of B_L, thus that of the local kinetic energy, though this is not a necessary condition since clouds with the same value of B may have different distributions of B_L.

The scaling of the kinetic energy (C 2) implies that the bubble cloud with larger values of B tends to induce a larger amount of kinetic energy in the liquid, with the same values of $(R_L, \dot{R}_L)$. Conversely, bubble clouds with a larger value of B need smaller values of $(R_L, \dot{R}_L)$ to induce the same amount of kinetic energy. This qualitatively implies that, with the same amplitude of pressure excitation, bubbles in a bubble cloud with a larger B (or B_0) tend to grow less, compared to a single, isolated bubble and bubble clouds with smaller values of B. The suppression of bubble/bubble cloud growth with a large value of B, thus inter-bubble interactions, has been observed in numerical simulation by Chahine (1983) and Wang & Brennen (1999), and in experiment by Bremond *et al.* (2006), and also qualitatively agrees with the results of the present simulations, in that bubble clouds present smaller differences in the moments, compared to differences in their values of B_0 (figures 8, 9 and 13).

https://doi.org/10.1017/jfm.2018.968 Published online by Cambridge University Press

REFERENCES

ANDO, K., COLONIUS, T. & BRENNEN, C. E. 2011 Numerical simulation of shock propagation in a polydisperse bubbly liquid. *Intl J. Multiphase Flow* **37** (6), 596–608.

ARORA, M., OHL, C.-D. & LOHSE, D. 2007 Effect of nuclei concentration on cavitation cluster dynamics. *J. Acoust. Soc. Am.* **121** (6), 3432–3436.

BAILEY, M. R., MCATEER, J. A., PISHCHALNIKOV, Y. A., HAMILTON, M. F. & COLONIUS, T. 2006 Progress in lithotripsy research. *Acoust. Today* **2** (2), 18–29.

BIESHEUVEL, A. & VANWIJNGAARDEN, L. 1984 Two-phase flow equations for a dilute dispersion of gas bubbles in liquid. *J. Fluid Mech.* **148**, 301–318.

BREMOND, N., ARORA, M., OHL, C.-D. & LOHSE, D. 2006 Controlled multibubble surface cavitation. *Phys. Rev. Lett.* **96**, 224501.

BRENNEN, C. E. 2002 Fission of collapsing cavitation bubbles. *J. Fluid Mech.* **472**, 153–166.

CAFLISCH, R. E., MIKSIS, M. J., PAPANICOLAOU, G. C. & TING, L. 1985 Effective equations for wave propagation in bubbly liquids. *J. Fluid Mech.* **153**, 259–273.

CANNEY, M. S., BAILEY, M. R., CRUM, L. A., KHOKHLOVA, V. A. & SAPOZHNIKOV, O. A. 2008 Acoustic characterization of high intensity focused ultrasound fields: a combined measurement and modeling approach. *J. Acoust. Soc. Am.* **124** (4), 2406–2420.

CARSTENSEN, E. L. & FOLDY, L. L. 1947 Propagation of sound through a liquid containing bubbles. *J. Acoust. Soc. Am.* **19** (3), 481–501.

CASH, J. R. & KARP, A. H. 1990 A variable order Runge-Kutta method for initial value problems with rapidly varying right-hand sides. *ACM Trans. Math. Softw.* **16** (3), 201–222.

CHAHINE, G. L. 1983 Cloud cavitation: theory. In *Proc. 14th Symp. on Naval Hydrodynamics, Washington, DC, USA*, pp. 165–194.

COLEMAN, A. J., SAUNDERS, J. E., CRUM, L. A. & DYSON, M. 1987 Acoustic cavitation generated by an extracorporeal shockwave lithotripter. *Ultrasound Med. Biol.* **13** (2), 69–76.

COMMANDER, K. W. & PROSPERETTI, A. 1989 Linear pressure waves in bubbly liquids: comparison between theory and experiments. *J. Acoust. Soc. Am.* **85** (2), 732–746.

CORALIC, V. & COLONIUS, T. 2014 Finite-volume WENO scheme for viscous compressible multicomponent flows. *J. Comput. Phys.* **274**, 95–121.

D'AGOSTINO, L. & BRENNEN, C. E. 1989 Linearized dynamics of spherical bubble clouds. *J. Fluid Mech.* **199**, 155–176.

DOINIKOV, A. A. 2004 Mathematical model for collective bubble dynamics in strong ultrasound fields. *J. Acoust. Soc. Am.* **116** (2), 821–827.

FUSTER, D. & COLONIUS, T. 2011 Modelling bubble clusters in compressible liquids. *J. Fluid Mech.* **688**, 352–389.

IKEDA, T., YOSHIZAWA, S., MASATAKA, T., ALLEN, J. S., TAKAGI, S., OHTA, N., KITAMURA, T. & MATSUMOTO, Y. 2006 Cloud cavitation control for lithotripsy using high intensity focused ultrasound. *Ultrasound Med. Biol.* **32** (9), 1383–1397.

ILINSKII, Y. A., HAMILTON, M. F. & ZABOLOTSKAYA, E. A. 2007 Bubble interaction dynamics in Lagrangian and Hamiltonian mechanics. *J. Acoust. Soc. Am.* **121** (2), 786–795.

ISHIMARU, A. 1978 *Wave Propagation and scattering in Random Media*, vol. 2. Academic Press.

JOHNSEN, E. & COLONIUS, T. 2009 Numerical simulations of non-spherical bubble collapse. *J. Fluid Mech.* **629**, 231–262.

KAMEDA, M. & MATSUMOTO, Y. 1996 Shock waves in a liquid containing small gas bubbles. *Phys. Fluids* **8** (2), 322–335.

KELLER, J. B. & MIKSIS, M. 1980 Bubble oscillations of large amplitude. *J. Acoust. Soc. Am.* **68** (2), 628–633.

LU, Y., KATZ, J. & PROSPERETTI, A. 2013 Dynamics of cavitation clouds within a high-intensity focused ultrasonic beam. *Phys. Fluids* **25** (7), 073301.

MA, J., CHAHINE, G. L. & HSIAO, C.-T. 2015 Spherical bubble dynamics in a bubbly medium using an Euler–Lagrange model. *Chem. Engng Sci.* **128**, 64–81.

MA, J., HSIAO, C. H. & CHAHINE, G. L. 2018 Numerical study of acoustically driven bubble cloud dynamics near a rigid wall. *Ultrasonics Sonochem.* **40** (Part A), 944–954.

https://doi.org/10.1017/jfm.2018.968 Published online by Cambridge University Press

MAEDA, K. & COLONIUS, T. 2017 A source term approach for generation of one-way acoustic waves in the Euler and Navier–Stokes equations. *Wave Motion* **75**, 36–49.

MAEDA, K. & COLONIUS, T. 2018 Eulerian–Lagrangian method for simulation of cloud cavitation. *J. Comput. Phys.* **371**, 994–1017.

MAEDA, K., KREIDER, W., MAXWELL, A., CUNITZ, B., COLONIUS, T. & BAILEY, M. 2015 Modeling and experimental analysis of acoustic cavitation bubbles for burst wave lithotripsy. *J. Phys.: Conf. Ser.* **656** (1), 012027.

MATSUMOTO, Y., ALLEN, J. S., YOSHIZAWA, S., IKEDA, T. & KANEKO, Y. 2005 Medical ultrasound with microbubbles. *Exp. Therm. Fluid Sci.* **29** (3), 255–265.

MATSUMOTO, Y. & YOSHIZAWA, S. 2005 Behaviour of a bubble cluster in an ultrasound field. *Intl J. Numer. Meth. Fluids* **47** (6–7), 591–601.

MAXWELL, A. D., CUNITZ, B. W., KREIDER, W., SAPOZHNIKOV, O. A., HSI, R. S., HARPER, J. D., BAILEY, M. R. & SORENSEN, M. D. 2015 Fragmentation of urinary calculi *in vitro* by burst wave lithotripsy. *J. Urol.* **193** (1), 338–344.

MCATEER, J. A., BAILEY, M. R., WILLIAMS, J. C. JR, CLEVELAND, R. O. & EVAN, A. P. 2005 Strategies for improved shock wave lithotripsy. *Minerva urologica e nefrologica = The Italian Journal of Urology and Nephrology* **57** (4), 271–287.

MENIKOFF, R. & PLOHR, B. J. 1989 The Riemann problem for fluid flow of real materials. *Rev. Mod. Phys.* **61** (1), 75.

MILLER, D. L., SMITH, N. B., BAILEY, M. R., CZARNOTA, G. J., HYNYNEN, K., MAKIN, I. R. S. & OF THE AMERICAN INSTITUTE OF ULTRASOUND IN MEDICINE, BIOEFFECTS COMMITTEE 2012 Overview of therapeutic ultrasound applications and safety considerations. *J. Ultrasound Med.* **31** (4), 623–634.

MØRCH, K. A. 1980 On the collapse of cavity clusters in flow cavitation. In *Cavitation and Inhomogeneities in Underwater Acoustics*, pp. 95–100. Springer.

MØRCH, K. A. 1982 Energy considerations on the collapse of cavity clusters. In *Mechanics and Physics of Bubbles in Liquids*, pp. 313–321. Springer.

OMTA, R. 1987 Oscillations of a cloud of bubbles of small and not so small amplitude. *J. Acoust. Soc. Am.* **82** (3), 1018–1033.

PISHCHALNIKOV, Y. A., SAPOZHNIKOV, O. A., BAILEY, M. R., WILLIAMS, J. C. JR, CLEVELAND, R. O., COLONIUS, T., CRUM, L. A., EVAN, A. P. & MCATEER, J. A. 2003 Cavitation bubble cluster activity in the breakage of kidney stones by lithotripter shockwaves. *J. Endourol.* **17** (7), 435–446.

PRESTON, A. T., COLONIUS, T. & BRENNEN, C. E. 2007 A reduced-order model of diffusive effects on the dynamics of bubbles. *Phys. Fluids* **19**, 123302.

PROSPERETTI, A., CRUM, L. A. & COMMANDER, K. W. 1988 Nonlinear bubble dynamics. *J. Acoust. Soc. Am.* **83** (2), 502–514.

RASTHOFER, U., WERMELINGER, F., HADIJDOUKAS, P. & KOUMOUTSAKOS, P. 2017 Large scale simulation of cloud cavitation collapse. *Procedia Comput. Sci.* **108** (Supplement C), 1763–1772.

REISMAN, G. E., WANG, Y.-C. & BRENNEN, C. E. 1998 Observations of shock waves in cloud cavitation. *J. Fluid Mech.* **355**, 255–283.

ROSSINELLI, D., HEJAZIALHOSSEINI, B., HADJIDOUKAS, P., BEKAS, C., CURIONI, A., BERTSCH, A., FUTRAL, S., SCHMIDT, S. J., ADAMS, N. A. & KOUMOUTSAKOS, P. 2013 11 pflop/s simulations of cloud cavitation collapse. In *SC '13 Proceedings of the International Conference on High Performance Computing, Networking, Storage and Analysis*, pp. 1–13. IEEE.

SHIMADA, M., MATSUMOTO, Y. & KOBAYASHI, T. 2000 Influence of the nuclei size distribution on the collapsing behavior of the cloud cavitation. *JSME Intl J.* B **43** (3), 380–385.

SHYUE, K.-M. 1998 An efficient shock-capturing algorithm for compressible multicomponent problems. *J. Comput. Phys.* **142** (1), 208–242.

STRIDE, E. P. & COUSSIOS, C. C. 2010 Cavitation and contrast: the use of bubbles in ultrasound imaging and therapy. *Proc. Inst. Mech. Engrs* H*: J. Engng Med.* **224** (2), 171–191.

TAKAHIRA, H., AKAMATSU, A. & FUJIKAWA, S. 1994 Dynamics of a cluster of bubbles in a liquid: theoretical analysis. *JSME Intl J.* B **37** (2), 297–305.

https://doi.org/10.1017/jfm.2018.968 Published online by Cambridge University Press

TANGUAY, M. 2003 Computation of bubbly cavitating flow in shock wave lithotripsy. PhD thesis, California Institute of Technology; http://resolver.caltech.edu/CaltechETD:etd-05282004-130028.

TIWARI, A., PANTANO, C. & FREUND, J. B. 2015 Growth-and-collapse dynamics of small bubble clusters near a wall. *J. Fluid Mech.* **775**, 1–23.

TOMITA, Y. & SHIMA, A. 1986 Mechanisms of impulsive pressure generation and damage pit formation by bubble collapse. *J. Fluid Mech.* **169**, 535–564.

VANWIJNGAARDEN, L. 1968 On the equations of motion for mixtures of liquid and gas bubbles. *J. Fluid Mech.* **33** (3), 465–474.

WANG, Y.-C. & BRENNEN, C. E. 1994 Shock wave development in the collapse of a cloud of bubbles. In *Cavitation and Multiphase Flow*, pp. 15–19. American Society of Mechanical Engineers.

WANG, Y.-C. & BRENNEN, C. E. 1999 Numerical computation of shock waves in a spherical cloud of cavitation bubbles. *Trans. ASME J. Fluids Engng* **121** (4), 872–880.

YOSHIZAWA, S., IKEDA, T., ITO, A., OTA, R., TAKAGI, S. & MATSUMOTO, Y. 2009 High intensity focused ultrasound lithotripsy with cavitating microbubbles. *Med. Biol. Engng Comput.* **47** (8), 851–860.

ZERAVCIC, Z., LOHSE, D. & VAN SAARLOOS, W. 2011 Collective oscillations in bubble clouds. *J. Fluid Mech.* **680**, 114–149.

https://doi.org/10.1017/jfm.2018.968 Published online by Cambridge University Press